Revisiting the decoupling limit of the Georgi-Machacek model with a scalar singlet

Geneviève Bélanger [a] **Juhi Dutta** [b] **Rohini M. Godbole** [c] **Sabine Kraml** [d]
Manimala Mitra [e,f] **Rojalin Padhan** [g] **and Abhishek Roy** [e,f]

[a] *LAPTh, CNRS, USMB,*
  9 Chemin de Bellevue, 74940 Annecy, France

[b] *Homer L. Dodge Department of Physics and Astronomy, University of Oklahoma,*
  Norman, OK 73019, U.S.A.

[c] *Centre for High Energy Physics, Indian Institute of Science,*
  Bengaluru - 560012, India

[d] *Université Grenoble Alpes, CNRS, Grenoble INP, LPSC-IN2P3,*
  38000 Grenoble, France

[e] *Institute of Physics, Sachivalaya Marg,*
  Bhubaneswar, Odisha 751005, India

[f] *Homi Bhabha National Institute, BARC Training School Complex,*
  Anushakti Nagar, Mumbai 400094, India

[g] *Department of Physics, Chung-Ang University,*
  Seoul 06974, Korea

  E-mail: belanger@lapth.cnrs.fr, juhi.dutta@ou.edu, rohini@iisc.ac.in,
  sabine.kraml@lpsc.in2p3.fr, manimala@iopb.res.in,
  rojalinpadhan2014@gmail.com, abhishek.r@iopb.res.in

ABSTRACT: We study the connection between collider and dark matter phenomenology in the singlet extension of the Georgi-Machacek model. In this framework, the singlet scalar serves as a suitable thermal dark matter (DM) candidate. Our focus lies on the region $v_\chi < 1\,\mathrm{GeV}$, where v_χ is the common vacuum expectation value of the neutral components of the scalar triplets of the model. Setting bounds on the model parameters from theoretical, electroweak precision and LHC experimental constraints, we find that the BSM Higgs sector is highly constrained. Allowed values for the masses of the custodial fiveplets, triplets and singlet are restricted to the range $140\,\mathrm{GeV} < M_{H_5^0} < 350\,\mathrm{GeV}$, $150\,\mathrm{GeV} < M_{H_3^0} < 270\,\mathrm{GeV}$ and $145\,\mathrm{GeV} < M_H < 300\,\mathrm{GeV}$. The extended scalar sector provides new channels for DM annihilation into BSM scalars that allow to satisfy the observed relic density constraint while being consistent with direct DM detection limits. The allowed region of the parameter space of the model can be explored in the upcoming DM detection experiments, both direct and indirect. In particular, the possible high values of $\mathrm{BR}(H_5^0 \to \gamma\gamma)$ can lead to an indirect DM signal within the reach of CTA. The same feature also provides the possibility of exploring

the model at the High-Luminosity run of the LHC. In a simple cut-based analysis, we find that a signal of about 4σ significance can be achieved in final states with at least two photons for one of our benchmark points.

Contents

1 Introduction

There are compelling motivations for considering models of new physics, as the Standard Model (SM) is inadequate to explain a few of the major observations in nature, such as, the observed non-zero neutrino masses and their mixings, the measured relic abundance of the dark matter (DM), and the observed matter-antimatter asymmetry of the universe. Furthermore, since the discovery of the 125 GeV SM scalar at the LHC [1, 2], it is yet unknown if the electroweak symmetry breaking (EWSB) is achieved by a single or multiple scalar fields. Several extensions have been studied in the literature to address this key question, among which the Georgi-Machacek (GM) model [3] is one of the most interesting extensions of the SM with two $SU(2)_L$ triplet scalar multiplets.

The scalar sector of the GM model consists of one real triplet with $Y = 0$ and one complex triplet with $Y = 2$ in addition to the SM Higgs doublet. The model preserves custodial symmetry (CS) at the tree level, but hypercharge interactions induce CS violation at one loop, thus leading to a correction to the ρ parameter [4]. These corrections are moderate because of the underlying tree-level CS. The model also predicts a larger Higgs-to-vector-boson coupling than in the SM, thus favouring a larger Higgs-to-diphoton rate. The scalar sector consists of ten physical degrees of freedom: a fiveplet, a triplet and two CP-even singlets under the CS. The Higgs and BSM phenomenology of this model have extensively been studied in [4–23]. One simplified version of the GM potential with a Z_2 symmetry that excludes the

two dimension-3 operators, has been studied in [4, 5, 9, 12, 14, 24]. The model also offers the possibility of generating naturally light Majorana masses for the neutrinos through the seesaw mechanism [10]. However, this minimal version of the model is inadequate to provide a viable stable DM candidate. This drawback of the model can be overcome by incorporating an additional isospin singlet scalar field, which transforms as $S \to -S$ under a Z_2 symmetry [16].

Amongst the various extensions of the SM that can incorporate DM, models containing a SM gauge singlet scalar field are the simplest extensions. The singlet scalar extension can easily accommodate a viable WIMP DM candidate [25–27], owing to its quartic interaction with the SM Higgs field. The minimal model, containing only a singlet, is however severely constrained by the precise determination of the DM relic density and the non-observation of DM through direct detection, since both depend directly on the coupling of DM to the SM-like Higgs boson [28]. Adding new particles (scalars, fermions or vector bosons) allows one to alleviate these constraints by disconnecting the processes that are responsible for elastic scattering on nuclei through Higgs exchange from the ones that contribute to DM annihilation in the early Universe. In particular, a more elaborate scalar sector, such as the BSM scalars present in the GM model makes it easier to satisfy current constraints by providing new final states for DM annihilation.

In this article, we consider the most general scalar potential of the GM model [7, 10, 13, 15, 16] extended by a real singlet scalar [16], which will be our DM candidate. We refer to this model as GM-S model henceforth. We focus on the decoupling limit [10, 15] of the GM-S model, which can be realised for a very small triplet vev. In this limit, the coupling strengths of the observed Higgs boson resemble their SM values. We revisit the validity of the model with respect to theoretical constraints, precision measurements of the oblique parameters, measurements of the SM Higgs to diphoton rate and the recent results from searches for neutral and doubly charged scalars at the LHC. We show that theoretical bounds, in particular the perturbative unitarity condition for this decoupling limit force the masses of the BSM scalars to be of the order of the weak scale. The measured values of electroweak precision observables (EWPO) further constrain large mass splitting between the fiveplet and triplet states. The diphoton rate of the SM-like Higgs boson restricts the splitting between the fiveplet mass and one of the dimension-full parameters of the potential, while searches for a doubly charged Higgs decaying into a pair of $W^\pm$ bosons require the mass splitting between the fiveplet and the triplet to be larger than roughly $30\,\text{GeV}$. Finally, searches for a BSM resonance decaying into diphoton states impose a lower limit on the triplet vev for the mass scales under consideration.

Taking into account the updated constraints on the parameter space of the GM-S model in the decoupling limit, we determine the parameter space that satisfies DM constraints from relic density and direct detection. As expected, we find that annihilation channels into any of the BSM Higgs play an important role in DM formation once we impose the direct detection constraints. Including the contributions of all final states leading to photons, we show that indirect detection limits from FermiLAT do not constrain the model. The CTA experiment, however, has the potential to probe part of the parameter space. Finally, we show that the same large decay rate into diphotons, that can lead to a signal at CTA, may also be exploited in searches at the High-Luminosity run of the LHC (HL-LHC). Searches in multi-lepton channels, on the other hand, are more challenging.

The structure of this paper is as follows: section 2 gives a brief review of the GM-S model. Theoretical and experimental constraints on the parameter space are discussed in section 3. The dark matter phenomenology is investigated in section 4, and the prospects for discovering the BSM scalars at the HL-LHC in section 5. A summary and conclusions are given in section 6. The appendix gives expressions for the partial decay widths of all the BSM scalars.

2 The model

The GM-S model we consider here is the original Georgi-Machacek (GM) model [3] extended by a real scalar field S [16]. The original GM model consists of an extended scalar sector which, in addition to the SM scalar doublet Φ, contains two scalar triplets $\xi = (\xi^+, \xi^0, \xi^-)^T$ and $\chi = (\chi^{++}, \chi^+, \chi^0)^T$. The triplet ξ has hypercharge $Y = 0$ while χ has hypercharge $Y = 2$. The neutral fields of both the doublet and the triplets acquire vevs $\langle \phi^0 \rangle = v_\phi / \sqrt{2}$, $\langle \xi^0 \rangle = v_\xi$ and $\langle \chi^0 \rangle = v_\chi$. The vev $\langle \phi^0 \rangle$ breaks the electroweak symmetry spontaneously, along with contributions from ξ^0 and χ^0.

The scalar potential is symmetric under a global $SU(2)_L \times SU(2)_R$ transformation which, after electroweak symmetry breaking, breaks down to a custodial symmetry $SU(2)_C$. At the tree level CS is guaranteed by demanding

$$\langle \xi^0 \rangle = \langle \chi^0 \rangle = v_\chi. \tag{2.1}$$

In order to make the global $SU(2)_L \times SU(2)_R$ symmetry explicit in the potential, we follow the convention of [15], and write the scalar fields in terms of a bi-doublet Φ and a bi-triplet X as follows:

$$\Phi = \begin{bmatrix} \phi^{0*} & \phi^+ \\ -\phi^- & \phi^0 \end{bmatrix}, \quad X = \begin{bmatrix} \chi^{0*} & \xi^+ & \chi^{++} \\ -\chi^- & \xi^0 & \chi^+ \\ \chi^{--} & -\xi^- & \chi^0 \end{bmatrix}. \tag{2.2}$$

As mentioned before in the GM-S model, in addition to the triplet fields ξ and χ, the model is further extended by a real scalar field S [16], which serves as the DM candidate. The stability of the DM is ensured by imposing a Z_2 symmetry, under which the DM is odd and all the other particles are even. Note that, the neutral scalar states from the X field, ξ^0 and χ^0, cannot be considered as DM candidates due to the lack of a discrete symmetry which can stabilize it. The general gauge-invariant tree-level scalar potential with Φ, X and S obeying CS has the form [5, 15]:

$$
\begin{aligned}
V(\Phi, X, S) = {} & \frac{\mu_2^2}{2} \mathrm{Tr}\left[\Phi^\dagger \Phi\right] + \frac{\mu_3^2}{2} \mathrm{Tr}\left[X^\dagger X\right] + \lambda_1 \left(\mathrm{Tr}\left[\Phi^\dagger \Phi\right]\right)^2 \\
& + \lambda_2 \mathrm{Tr}\left[\Phi^\dagger \Phi\right] \mathrm{Tr}\left[X^\dagger X\right] + \lambda_3 \mathrm{Tr}\left[X^\dagger X X^\dagger X\right] \\
& + \lambda_4 \left(\mathrm{Tr}\left[X^\dagger X\right]\right)^2 - \lambda_5 \mathrm{Tr}\left[\Phi^\dagger \tau^a \Phi \tau^b\right] \mathrm{Tr}\left[X^\dagger t^a X t^b\right] \\
& - M_1 \mathrm{Tr}\left[\Phi^\dagger \tau^a \Phi \tau^b\right] \left(U X U^\dagger\right)_{ab} - M_2 \mathrm{Tr}\left[X^\dagger t^a X t^b\right] \left(U X U^\dagger\right)_{ab} + V(S),
\end{aligned}
\tag{2.3}
$$

where $\tau^a = \sigma^a/2$ with σ^a being the Pauli matrices; t^a are generators of the adjoint representation and the matrix

$$U = \begin{bmatrix} -\frac{1}{\sqrt{2}} & 0 & \frac{1}{\sqrt{2}} \\ -\frac{i}{\sqrt{2}} & 0 & -\frac{i}{\sqrt{2}} \\ 0 & 1 & 0 \end{bmatrix} \tag{2.4}$$

is used to rotate the bi-triplet into a cartesian basis [7]. In eq. (2.3), $V(S)$ contains the terms involving the field S and has the form

$$V(S) = \frac{\mu_S^2}{2} S^2 + \lambda_a\, S^2\, \mathrm{Tr}\left(\Phi^\dagger\Phi\right) + \lambda_b\, S^2\, \mathrm{Tr}\left[X^\dagger X\right] + \lambda_S S^4\,. \tag{2.5}$$

In addition to the couplings λ_i in eq. (2.3) that represent the quartic interaction of the Φ, X fields and the interaction between Φ and X, the interaction terms with couplings M_1 and M_2 govern the tri-linear interactions between Φ and X and the self-interactions of the X fields, respectively.

The field χ, being a complex triplet with hypercharge $Y = 2$, also interacts with the lepton doublets L through the Yukawa Lagrangian

$$\mathcal{L}_\nu = Y_\nu \bar{L}^c i\tau_2 \chi L + \text{h.c.}. \tag{2.6}$$

Note that the above term together with the tri-linear M_2 term in eq. (2.3) violates lepton number and hence can generate the Majorana masses of the light neutrinos. The light neutrino mass matrix can be expressed in terms of the Yukawa coupling Y_ν and the vev v_χ as follows

$$M_\nu = Y_\nu v_\chi = U_{\text{PMNS}}^* M_\nu^d U_{\text{PMNS}}^\dagger\,, \tag{2.7}$$

where U_{PMNS} is the diagonalization matrix for the light neutrinos, and $M_\nu^d = \text{diag}(m_1, m_2, m_3)$ are the neutrino masses.

2.1 The scalar spectrum

To obtain the scalar spectrum in the physical mass basis, one needs to impose the minimisation conditions

$$\frac{\partial V}{\partial v_\phi} = v_\phi \left[\mu_2^2 + 4\lambda_1 v_\phi^2 + 3\left(2\lambda_2 - \lambda_5\right) v_\chi^2 - \frac{3}{2} M_1 v_\chi \right] = 0\,, \tag{2.8}$$

$$\frac{\partial V}{\partial v_\chi} = 3\mu_3^2 v_\chi + 3\left(2\lambda_2 - \lambda_5\right) v_\phi^2 v_\chi + 12\left(\lambda_3 + 3\lambda_4\right) v_\chi^3 - \frac{3}{4} M_1 v_\phi^2 - 18 M_2 v_\chi^2 = 0\,. \tag{2.9}$$

Both the doublet and triplet vevs are responsible for the W/Z-boson mass generation,

$$M_W^2 = M_Z^2 \cos^2\theta_W = \frac{g^2 v^2}{4} = \frac{g^2}{4}\left(v_\phi^2 + 8 v_\chi^2\right), \tag{2.10}$$

where $v = 246\,\text{GeV}$ and g is the coupling constant of the $\text{SU}(2)_L$ gauge group. Based upon the transformation properties under the custodial $\text{SU}(2)_C$ symmetry, the physical scalar

states can be categorised into a fiveplet, a triplet and two CP-even singlets. The fiveplet scalars are expressed in the form:

$$H_5^{++} = \chi^{++}, \quad H_5^+ = \frac{1}{\sqrt{2}}\left(\chi^+ - \xi^+\right), \quad H_5^0 = \sqrt{\frac{2}{3}}\,\xi^{0,r} - \sqrt{\frac{1}{3}}\,\chi^{0,r}, \tag{2.11}$$

where $\xi^{0,r}$ and $\chi^{0,r}$ represent the real components of ξ^0 and χ^0, respectively. Similarly, the triplet scalar states can be expressed as

$$H_3^+ = -s_H\,\phi^+ + \frac{1}{\sqrt{2}}c_H\left(\xi^+ + \chi^+\right), \quad H_3^0 = -s_H\,\phi^{0,i} + c_H\,\chi^{0,i}, \tag{2.12}$$

with $\phi^{0,i}$ and $\chi^{0,i}$ being the imaginary components of ϕ^0 and χ^0, respectively. The mixing angle corresponding to $H_3^\pm$ and H_3^0 states can be written as

$$c_H \equiv \cos\theta_H = \frac{v_\phi}{v}, \quad s_H \equiv \sin\theta_H = \frac{2\sqrt{2}v_\chi}{v}. \tag{2.13}$$

Using the minimization conditions in eqs. (2.8), (2.9), we obtain

$$M_{H_5}^2 = \frac{M_1}{4v_\chi}v_\phi^2 + 12M_2 v_\chi + \frac{3}{2}\lambda_5 v_\phi^2 + 8\lambda_3 v_\chi^2, \tag{2.14}$$

and

$$M_{H_3}^2 = \left(\frac{M_1}{4v_\chi} + \frac{\lambda_5}{2}\right)v^2. \tag{2.15}$$

M_{H_5} and M_{H_3} are the masses of the fiveplet and the triplet fields. The mass of the gauge singlet field S is given by

$$M_S^2 = \mu_S^2 + 2\lambda_a v_\phi^2 + 6\lambda_b v_\chi^2. \tag{2.16}$$

The neutral components of the $SU(2)_L$ doublet and triplets mix, leading to two CP-even $SU(2)_C$ singlets (h, H),

$$\begin{aligned}
h &= c_\alpha \phi^{0,r} - s_\alpha H_1^{0'}, \\
H &= s_\alpha \phi^{0,r} + c_\alpha H_1^{0'},
\end{aligned} \tag{2.17}$$

where $H_1^{0'}$ is defined as

$$H_1^{0'} = \sqrt{\frac{1}{3}}\,\xi^{0,r} + \sqrt{\frac{2}{3}}\,\chi^{0,r}. \tag{2.18}$$

The mixing angle α and the mass eigenvalues are obtained by diagonalisation of the 2×2 mass-squared matrix corresponding to these scalars. This matrix reads

$$\mathcal{M}^2 = \begin{bmatrix} \mathcal{M}_{11}^2 & \mathcal{M}_{12}^2 \\ \mathcal{M}_{12}^2 & \mathcal{M}_{22}^2 \end{bmatrix} \tag{2.19}$$

with

$$\begin{aligned}
\mathcal{M}_{11}^2 &= 8\lambda_1 v_\phi^2, \\
\mathcal{M}_{12}^2 &= \frac{\sqrt{3}}{2}v_\phi[-M_1 + 4(2\lambda_2 - \lambda_5)v_\chi], \\
\mathcal{M}_{22}^2 &= \frac{M_1 v_\phi^2}{4v_\chi} - 6M_2 v_\chi + 8(\lambda_3 + 3\lambda_4)v_\chi^2.
\end{aligned} \tag{2.20}$$

The mixing angle α between h and H, and the respective mass eigenvalues are given by

$$\tan 2\alpha = \frac{2\mathcal{M}_{12}^2}{\mathcal{M}_{22}^2 - \mathcal{M}_{11}^2}\,, \tag{2.21}$$

$$M_{H,h}^2 = \frac{1}{2}\left[\mathcal{M}_{11}^2 + \mathcal{M}_{22}^2 \pm \sqrt{(\mathcal{M}_{11}^2 - \mathcal{M}_{22}^2)^2 + 4(\mathcal{M}_{12}^2)^2}\right], \tag{2.22}$$

where we assume $M_H^2 > M_h^2$. In our subsequent analysis, we consider h as the $125\,\text{GeV}$ SM-like Higgs boson while H is a heavier BSM scalar.

The dimensionless couplings in the scalar potential, $\lambda_{1,\ldots,5}$, can be expressed in terms of the physical parameters M_{H_5}, M_{H_3}, M_H, M_h and α as follows:

$$\begin{aligned}
\lambda_1 &= \frac{1}{8v^2 c_H^2}(M_h^2 c_\alpha^2 + M_H^2 s_\alpha^2)\,, \\
\lambda_2 &= \frac{1}{6v^2 s_H c_H}\left[\frac{\sqrt{6}}{2}s_{2\alpha}(M_h^2 - M_H^2) + 3s_H c_H(2M_{H_3}^2 - \widetilde{M_1^2})\right], \\
\lambda_3 &= \frac{1}{v^2 s_H^2}\left[c_H^2(2\widetilde{M_1^2} - 3M_{H_3}^2) + M_{H_5}^2 - M^2\right], \\
\lambda_4 &= \frac{1}{6v^2 s_H^2}\left[2M_H^2 c_\alpha^2 + 2M_h^2 s_\alpha^2 + 3M^2 - 2M_{H_5}^2 + 6c_H^2(M_{H_3}^2 - \widetilde{M_1^2})\right], \\
\lambda_5 &= -\frac{2}{v^2}(\widetilde{M_1^2} - M_{H_3}^2)\,,
\end{aligned} \tag{2.23}$$

where s_H and c_H are defined in eq. (2.13) and

$$\widetilde{M_1^2} \equiv \frac{v}{\sqrt{2}s_H}M_1\,, \quad M^2 \equiv 3\sqrt{2}s_H v M_2\,. \tag{2.24}$$

A few observations about the behaviour of various quantities in the limit of a small v_χ, a case we will discuss in detail in the next section, are in order. For a small v_χ leading to the limit $s_H \to 0$ (see eq. (2.13)) in order to assure that $\widetilde{M_1^2}$ remains finite we need to assume that $M_1 \to 0$. Moreover, in this limit, it follows from eq. (2.24) that a finite value for M implies a very large value of M_2, eventually leading to very large couplings and violation of perturbativity. Note that, in the $s_H \to 0$ limit, the quartic couplings $\lambda_{2,4}$ diverge unless s_α is set to 0. This then implies complete decoupling of the scalar H from the SM Higgs state h in this limit.

2.2 The case of small v_χ

A number of studies have focused on relatively high triplet vev $v_\chi > 1\,\text{GeV}$ [12, 17, 20, 21, 29–35]. The main objective of this paper is to analyse the Higgs and DM phenomenology for a low value of the triplet vev, $v_\chi \lesssim 1\,\text{GeV}$ For a small v_χ, the decoupling limit characterised by $v_\chi \to 0$ ($s_H \to 0$) along with $s_\alpha \to 0$ can be realised. For a small v_χ, the expression of the fiveplet mass simplifies to

$$M_{H_5}^2 \simeq \frac{3}{2}\lambda_5 v^2 + \widetilde{M_1^2} + M^2\,. \tag{2.25}$$

With the additional condition $\sin\alpha = 0$, required to get rid of the divergence in the λ couplings (eq. (2.23)) for $s_H \to 0$, we obtain for the singlet masses

$$M_H^2 \simeq \widetilde{M_1^2} - \frac{1}{2}M^2\,, \quad M_h^2 \simeq 8\lambda_1 v^2\,. \tag{2.26}$$

Substituting λ_5 from eq. (2.23) and M_H from eq. (2.26) into eq. (2.25), we obtain

$$M_{H_5}^2 \simeq 3M_{H_3}^2 - 2M_H^2 \,. \tag{2.27}$$

In order to allow for a departure from $v_\chi = 0$ ($s_H = 0$), we introduce $\overline{M}$, a free parameter of mass dimension one. Then we can write M_H^2 and $\widetilde{M}_1^2$ as

$$M_H^2 = \frac{1}{2}\left(3M_{H_3}^2 - M_{H_5}^2 + 3s_H^2\overline{M}^2\right), \quad \widetilde{M}_1^2 = \frac{1}{2}\left(3M_{H_3}^2 - M_{H_5}^2 + M^2\right). \tag{2.28}$$

All the dimensionless couplings can then be rewritten as [10]

$$\lambda_1 = \frac{M_h^2}{8v^2c_H^2}\,, \qquad \lambda_2 = \frac{M_{H_3}^2 + M_{H_5}^2 - M^2}{4v^2}\,, \qquad \lambda_3 = \frac{M_{H_5}^2 - M^2}{v^2}\,,$$

$$\lambda_4 = \frac{M_{H_3}^2 - M_{H_5}^2 + M^2 + \overline{M}^2}{2v^2}\,, \qquad \lambda_5 = \frac{-(M_{H_3}^2 - M_{H_5}^2 + M^2)}{v^2}\,. \tag{2.29}$$

It is evident from eqs. (2.29) that with this parametrization all the v_χ dependence drops out and there are no apparent divergences in the λ's for $v_\chi \to 0$. It is also important to highlight that the off-diagonal element of the CP-even neutral mixing matrix $\mathcal{M}_{12}^2$ is identically zero in this parameterization (see eqs. (2.20)) and consequently $\sin\alpha \equiv 0$ (instead of $\sin\alpha \ll 1$).

In the following, we fix $m_h = 125\,\mathrm{GeV}$ and $\sin\alpha = 0$ and take

$$v_\chi,\ M_{H_3},\ M_{H_5},\ M,\ \overline{M}\,, \tag{2.30}$$

as free parameters. The value of M_H is then fixed by eqs. (2.28) and (2.13). The singlet scalar sector is characterised by free parameters M_S, λ_a, λ_b, λ_S. In this work, we consider the DM to be relatively heavy, so that invisible decays of h and H are kinematically forbidden. Moreover H_3 and H_5 states do not couple to DM pairs via cubic interaction as it violates the CS. Hence M_S, λ_a, λ_b, λ_S do not have any impact on collider searches and are only relevant for discussions of DM, only the parameters v_χ, M_{H_3}, M_{H_5}, M, $\overline{M}$ have direct influence on the collider searches.

Before concluding this section, we note that, for small values of v_χ, which is the focus of this study, the couplings of h to fermions are equal to those of the SM while its couplings to gauge bosons ($V = W^\pm, Z$) receive a small correction, $C_{hVV} = c_H C_{hVV}^{SM}$ [15, 36]. The heavy CP-even neutral scalar H does not couple to fermions as $\sin\alpha = 0$ and H_5^0 couples only to $\bar{\nu}\nu$. Their couplings to gauge bosons are suppressed by a factor s_H (see section 3 or appendix). The couplings of the CP-odd neutral scalar H_3^0 to fermions are also suppressed by a factor s_H. Explicit expressions for the trilinear couplings of the neutral scalars can be found in section 3.3. We refer the reader to [10, 15, 36] for a detailed description of all the couplings of the SM and BSM scalars of this model with SM fermions, gauge bosons, as well as with other BSM scalars.

3 Existing theoretical and experimental constraints

In this section, we assess the parameter space of the GM-S model that is consistent with existing theoretical constraints and experimental constraints from colliders. To this end, we perform a flat random scan over the free parameters $\{M_{H_3}, M_{H_5}, M, \overline{M}, v_\chi, \lambda_a, \lambda_b, \lambda_S\}$ within the ranges specified in table 1. About 4×10^6 data points are sampled in this scan and confronted against the constraints detailed below.

Parameter	Scanned range
M_{H_3} [GeV]	$[10^2, 10^3]$
M_{H_5} [GeV]	$[10^2, 10^3]$
M [GeV]	$[10^1, 10^3]$
$\overline{M}$ [GeV]	$[10^1, 10^6]$
v_χ [GeV]	$[10^{-4}, 10^0]$
$\lambda_a, \lambda_b, \lambda_S$	$[10^{-4}, 10^0]$
M_S [GeV]	$[10^2, 10^3]$

Table 1. Ranges of the input parameters that we use in our numerical scan together with $\sin\alpha = 0$.

Before proceeding, a comment is in order regarding the subset of parameters considered. As discussed in the previous section, $\lambda_{1,\dots,5}$ are expressed in terms of the physical scalar masses $M_h, M_{H_3}, M_{H_5}, M, \overline{M}$ and v_χ; together with the quartic couplings $\lambda_{a,b,S}$ they are subject to the condition of perturbative unitarity and potential being bounded from below. Hence, the entire subset $\{M_{H_3}, M_{H_5}, M, \overline{M}, v_\chi, \lambda_a, \lambda_b, \lambda_S\}$ is needed to check these and other theoretical constraints. In contrast, the DM mass M_S is relevant only for DM production and detection and therefore ignored in this section. The DM-related constraints, which will affect $M_S, \lambda_a, \lambda_b, \lambda_S$, will be discussed in section 4.

3.1 Theoretical constraints and constraints from oblique parameters

Perturbative unitarity

By the perturbative unitarity of the $2 \to 2$ scalar field scattering amplitudes, the scalar couplings in eq. (2.29) can be constrained. We take into account the following constraints on the quartic couplings of this model [16]

$$8\pi > \left| 12\lambda_1 + 14\lambda_3 + 22\lambda_4 \pm \sqrt{(12\lambda_1 - 14\lambda_3 - 22\lambda_4)^2 + 144\lambda_2^2} \right|,$$

$$8\pi > \left| 4\lambda_1 - 2\lambda_3 + 4\lambda_4 \pm \sqrt{(4\lambda_1 + 2\lambda_3 - 4\lambda_4)^2 + 4\lambda_5^2} \right|,$$

$$8\pi > |16\lambda_3 + 8\lambda_4|,$$

$$8\pi > |4\lambda_3 + 8\lambda_4|,$$

$$8\pi > |4\lambda_2 - \lambda_5|,$$

$$8\pi > |4\lambda_2 + 2\lambda_5|,$$

$$8\pi > |4\lambda_2 + 4\lambda_5|,$$

$$8\pi > |4\lambda_a|,$$

$$8\pi > |4\lambda_b|,$$

$$\lambda_S < \frac{1}{6}\left(4\pi + \frac{2\lambda_a^2(7\lambda_3 + 11\lambda_4 - \pi) + 9\lambda_b^2(3\lambda_1 - \pi) - 18\lambda_2\lambda_a\lambda_b}{2(7\lambda_3 + 11\lambda_4 - \pi)(3\lambda_1 - \pi) - 9\lambda_2^2}\right),$$

$$\lambda_S > \frac{1}{6}\left(-4\pi + \frac{2\lambda_a^2(7\lambda_3 + 11\lambda_4 + \pi) + 9\lambda_b^2(3\lambda_1 + \pi) - 18\lambda_2\lambda_a\lambda_b}{2(7\lambda_3 + 11\lambda_4 + \pi)(3\lambda_1 + \pi) - 9\lambda_2^2}\right). \tag{3.1}$$

The condition $|4\lambda_2 - \lambda_5| < 8\pi$ restricts the triplet mass to $M_{H_3} \lesssim 870\,\text{GeV}$. The conditions $|4\lambda_2 + 2\lambda_5| < 8\pi$ and $|4\lambda_2 + 4\lambda_5| < 8\pi$ do not allow arbitrary mass squared splitting between

$M_{H_5}^2$ and M^2 as $|M_{H_5}^2 - M^2|/v^2 \leq 4\pi$. $|4\lambda_3 + 8\lambda_4| < 8\pi$ leads to $|M_{H_3}^2 + \overline{M}^2|/v^2 \leq 2\pi$. As we will present later the conditions in eq. (3.1) jointly put stronger constraints on M_{H_3}.

Note that, the range of M_{H_3} given in table 1 together with the constraint $|M_{H_3}^2 + \overline{M}^2|/v^2 \leq 2\pi$ dictates that large values of $\overline{M} > \mathcal{O}(100)\,\text{GeV}$ will get discarded. Since s_H is also small, $s_H < \mathcal{O}(10^{-2})$, the term $3s_H^2\overline{M}^2$ in eq. (2.28) is negligible. The condition $M_H^2 > 0$ therefore implies $M_{H_5} \lesssim \sqrt{3}M_{H_3}$, which will be visible in the allowed points that satisfy the theory constraints. We note that out of the 4×10^6 data points that were sampled in the scan, about 3×10^6 points satisfy this condition.

Potential bounded from below

In order to ensure the potential is bounded from below, we implemented the conditions computed in refs. [15, 16] which are as follows,

$$
\begin{aligned}
\lambda_1 &> 0, \\
\lambda_4 &> \begin{cases} -\frac{1}{3}\lambda_3 & \text{for } \lambda_3 \geq 0, \\ -\lambda_3 & \text{for } \lambda_3 < 0, \end{cases} \\
\lambda_2 &> \begin{cases} \frac{1}{2}\lambda_5 - 2\sqrt{\lambda_1\left(\frac{1}{3}\lambda_3 + \lambda_4\right)} & \text{for } \lambda_5 \geq 0,\ \lambda_3 \geq 0, \\ \omega_+(\zeta)\lambda_5 - 2\sqrt{\lambda_1\left(\zeta\lambda_3 + \lambda_4\right)} & \text{for } \lambda_5 \geq 0,\ \lambda_3 < 0, \\ \omega_-(\zeta)\lambda_5 - 2\sqrt{\lambda_1\left(\zeta\lambda_3 + \lambda_4\right)} & \text{for } \lambda_5 < 0,\ \lambda_3 \in R \end{cases}
\end{aligned}
$$

$$
\begin{aligned}
\lambda_a &> -2\sqrt{\lambda_1\lambda_S}, \\
\lambda_b &> \begin{cases} -2\sqrt{\left(\frac{1}{3}\lambda_3 + \lambda_4\right)\lambda_S} & \text{for } \lambda_3 \geq 0, \\ -2\sqrt{(\lambda_3 + \lambda_4)\lambda_S} & \text{for } \lambda_3 < 0, \end{cases} \\
\lambda_S &> 0,
\end{aligned}
\tag{3.2}
$$

where ζ and ω satisfies the following range,

$$
\zeta \in \left[\frac{1}{3}, 1\right], \qquad \omega \in \left[-\frac{1}{4}, \frac{1}{2}\right].
\tag{3.3}
$$

For a given value of ζ, we can write $\omega \in [\omega_-, \omega_+]$, where [15]

$$
\omega_\pm(\zeta) = \frac{1}{6}(1-B) \pm \frac{\sqrt{2}}{3}\left[(1-B)\left(\frac{1}{2}+B\right)\right]^{\frac{1}{2}},
\tag{3.4}
$$

with

$$
B \equiv \sqrt{\frac{3}{2}\left(\zeta - \frac{1}{3}\right)} \in [0, 1].
\tag{3.5}
$$

Absence of deeper custodial symmetry-breaking minima

To ensure no deeper custodial symmetry-breaking minima in our chosen parameter space, we passed the allowed parameters from perturbative unitarity and bounded from the below condition through Vevacious [37] to check the global minima condition.
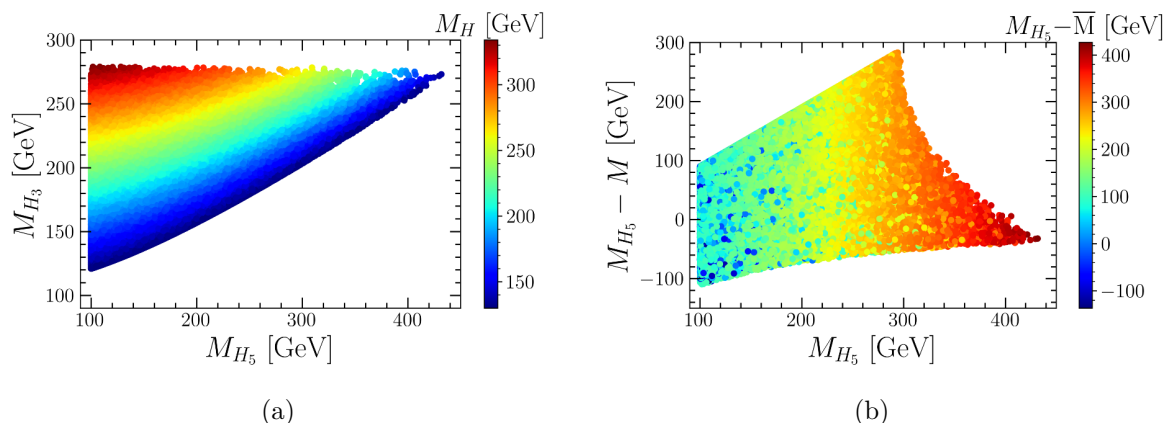
Figure 1. Points that satisfy theoretical constraints, such as perturbative unitarity, potential bounded from below and absence of deeper custodial symmetry breaking minima, mentioned in section 3.1: (a) in the plane M_{H_5} vs. M_{H_3} with the value of M_H shown in color and (b) in the M_{H_5} vs. $M_{H_5} - M$ plane with $M_{H_5} - \overline{M}$ shown in color.

Mass of CP-even BSM scalar

As we have discussed before, the positivity condition for the mass of the CP-even BSM scalar, M_H, discards the region where $\sqrt{3}M_{H_3} < M_{H_5}$. Among the SM and BSM Higgs states h, H, we demand that H is heavier than the SM Higgs so that it does not have any influence in the measurement of $h \to \gamma\gamma$ rate. We choose M_H value sufficiently larger than the SM Higgs mass, $M_H \geq 130\,\mathrm{GeV}$. Since s_H is almost negligible and the allowed value of $\overline{M}$ can at most be $\mathcal{O}(10^2)\,\mathrm{GeV}$, this in turn allows for $3M_{H_3}^2 - M_{H_5}^2 > \mathcal{O}(10^4)\,\mathrm{GeV}^2$, see eqs. (2.27) and (2.28).

The viable parameter space satisfying all the theoretical constraints in different planes is shown in figure 1. In figure 1(a), we show the allowed points in the M_{H_5} vs. M_{H_3} plane. The color code following eq. (2.28) indicates M_H. As can be seen, for our chosen scenario with a small v_χ and $\sin\alpha = 0$, TeV scale fiveplet and triplet scalar states are ruled out. All the perturbative unitarity conditions from eq. (3.1) jointly exclude $M_{H_3} > 280\,\mathrm{GeV}$ and $M_{H_5} > 435\,\mathrm{GeV}$ while the mass of the singlet scalar, H, is restricted to $M_H < 330\,\mathrm{GeV}$. The conditions on the potential to be bounded from below do not set additional limit on the parameters which pass the perturbative unitarity conditions. The condition on $M_H \geq 130\,\mathrm{GeV}$ largely excludes points in the lower right corner of the M_{H_5} vs. M_{H_3} plane as mentioned above. In figure 1(b) we show the allowed values for the differences $M_{H_5} - M$ and $M_{H_5} - \overline{M}$. The values of M and $\overline{M}$ are constrained to $M < 435\,\mathrm{GeV}$ and $\overline{M} < 250\,\mathrm{GeV}$. Moreover $|M_{H_5}^2 - M^2|/v^2 \lesssim 4\pi$ follows for the perturbativity constraint on the λ_3 coupling. After including the theory constraint with a small $v_\chi < 1\,\mathrm{GeV}$ and $\sin\alpha = 0$, it is evident that the independent parameters M_{H_5}, M_{H_3}, M and $\overline{M}$ are strongly constrained. The triplet vev v_χ and the mass of DM M_S, and couplings $\lambda_{a,b,s}$ are allowed over the full range considered.

Oblique parameters

The S parameter contributions in the GM model, relative to the SM are computed in [36]. They involve corrections to the SM diagrams contributions to the neutral bosons self-energy such as the Zh loop contribution that is proportional to v_χ/v together with new contributions
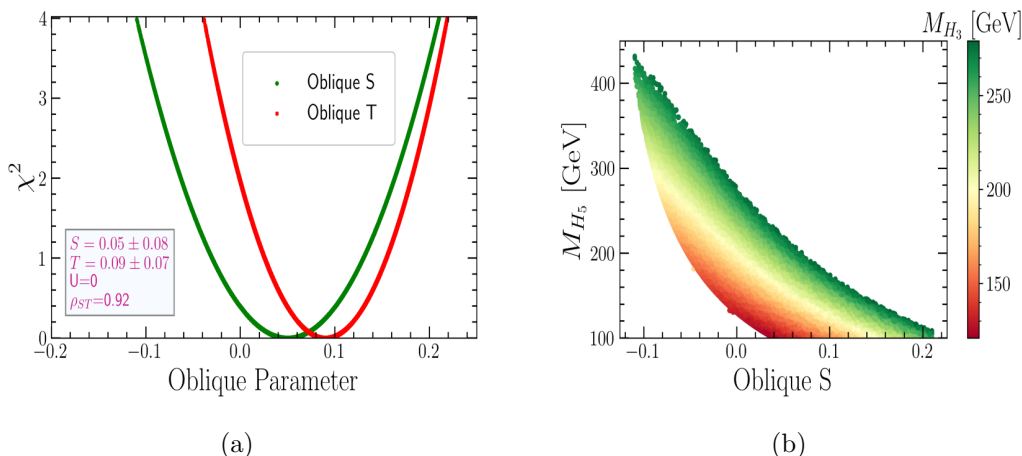
Figure 2. (a) Variation of χ^2 w.r.t. the oblique parameters, S (red line) and T (green line). (b) Points in the S vs. M_{H_5} plane that satisfy the constraint from oblique parameters as well as previously mentioned theoretical constraints. The color bar shows the value of M_{H_3}. In deriving the constraints, we assume $U = 0$.

to the Z boson self-energy that involve loops of two scalars HH_3, H_5H_3 and $H_5^{\pm}H_3^{\mp}$ with couplings of electroweak strength. Finally, new contributions involving two scalars, hH_3, or loops of one gauge boson and a scalar $ZH, ZH_5, W^{\pm}H_5^{\mp}$ are all suppressed by a factor v_{χ}/v. From the global electroweak fit [38] we have the measurements for S, T parameters

$$S_{\text{exp}} = 0.05 \pm 0.08, \qquad T_{\text{exp}} = 0.09 \pm 0.07, \qquad (3.6)$$

for the SM Higgs mass $M_h = 125\,\text{GeV}$, $U = 0$, and correlation $\rho_{ST} = +0.92$. We compute the χ^2 according to

$$\chi^2 = \frac{1}{(1 - \rho_{ST}^2)} \left[\frac{(S - S_{\text{exp}})^2}{(\Delta S_{\text{exp}})^2} + \frac{(T - T_{\text{exp}})^2}{(\Delta T_{\text{exp}})^2} - \frac{2\rho_{ST}(S - S_{\text{exp}})(T - T_{\text{exp}})}{\Delta S_{\text{exp}}\Delta T_{\text{exp}}} \right], \qquad (3.7)$$

where ΔS_{exp} and ΔT_{exp} are the 1σ experimental uncertainties. As hypercharge interactions break the custodial symmetry at one-loop level, the T parameter in the GM model has divergent value [4]. Therefore following ref. [36] we marginalise over the T parameter and set

$$T = T_{\text{exp}} + \rho_{ST}(S - S_{\text{exp}})\frac{\Delta T_{\text{exp}}}{\Delta S_{\text{exp}}}. \qquad (3.8)$$

In figure 2(a), we show the χ^2 distribution taking into account current experimental limits. In figure 2(b), we show the allowed values of M_{H_3} and M_{H_5} satisfying $\chi^2 < 4$ and the corresponding values of S. We expect the oblique parameters to constrain the mass difference between two scalars and in particular $M_{H_3} - M_{H_5}$. Indeed we find that almost all points that pass theoretical bound are also consistent with the measurements of the oblique parameters. Only points where the mass difference is large are excluded, they are found in the region $M_{H_5} \sim 100\,\text{GeV}$ and $M_{H_3} \geq 260\,\text{GeV}$. A summary of the different constraints that we consider in this work will be presented in figure 9.

3.2 Constraints on $\Gamma(H_i)/M_i$ for scalars

Before checking the current experimental limits on BSM scalars, we impose a constraint on the total $\Gamma(H_i)/M_i$ ratio for the neutral and charged scalars, where $\Gamma(H_i)$ represent the total decay width of the BSM scalar H_i and M_i represents its mass. Mainly tri-linear scalar couplings lead to large $\Gamma(H_i)/M_i$ for the neutral scalars H_5^0 and H in two ways: the first one is when scalars decay to two other scalars $H_i \rightarrow H_j H_j$ and the second one is when the tri-linear scalar couplings becomes large leading to an enhanced loop-induced partial with for $H_i \rightarrow V\gamma$ with $V = \gamma, Z$ states. This can happen when for a fixed value of M, v_χ becomes small.

The partial decay width of a CP-even neutral scalar H_i decaying into $2\gamma/Z\gamma$ is [17]

$$\Gamma(H_i \rightarrow V\gamma) = \frac{m_{H_i}^3}{32\pi\eta_V}\left[1 - \frac{M_V^2}{m_{H_i}^2}\right]^3 |S|^2, \tag{3.9}$$

where S is the form factor and $V = \gamma, Z$. Here η_V is a symmetry factor that accounts for identical particles in the final state, with $\eta_\gamma = 2$ and $\eta_Z = \eta_W = 1$. For the CP-even scalars h, H, and H_5^0, the form factor is[1]

$$S_{H_i\gamma\gamma} = \frac{\alpha_{\rm em}}{2\pi v}\left[\beta_W^{H_i} F_1(\tau_W) + \sum_f N_{cf}Q_f^2\beta_f^{H_i}F_{1/2}(\tau_f) + \sum_s \beta_s^{H_i}Q_s^2 F_0(\tau_s)\right], \tag{3.10}$$

where $N_{cf} = 3$ for quarks and 1 for leptons, Q_j is the electric charge of particle j in units of e, and the sums run over all fermions and scalars that can propagate in the loop for the parent scalar H_i. In this model, the charged scalars are $s = \{H_3^\pm, H_5^\pm, H_5^{++}, H_5^{--}\}$ and we only keep the top quark contribution to the fermion loop, $f = t$. The coupling coefficients $\beta_j^{H_i}$ are defined as,

$$\beta_W^{H_i} = \frac{C_{H_i W^+ W^-}e^2}{gM_W}, \qquad \beta_f^{H_i} = -\frac{C_{H_i f\bar{f}}v}{m_f}, \qquad \beta_s^{H_i} = \frac{C_{H_i ss}v}{2m_s^2}, \tag{3.11}$$

for a propagating W boson, fermion f, and scalar s, respectively. In the case of the W boson and fermion loops, these factors $\beta_{W,f}^{H_i}$ are equal to the usual ratios $\kappa_{W,f}^{H_i}$ of the scalar coupling to WW or $f\bar{f}$ normalized to the corresponding SM Higgs coupling as described in refs. [15, 17]. Note that $\beta_f^{H_5^0} = 0$ because the H_5 states are fermiophobic.

The loop factors are given in terms of the usual functions for particles of spin 0, 1/2 and 1 [39],

$$\begin{aligned} F_1(\tau_W) &= 2 + 3\tau_W + 3\tau_W(2 - \tau_W)f(\tau_W), \\ F_{1/2}(\tau_f) &= -2\tau_f[1 + (1 - \tau_f)f(\tau_f)], \\ F_0(\tau_s) &= \tau_s[1 - \tau_s f(\tau_s)], \end{aligned} \tag{3.12}$$

where $\tau_j = 4m_j^2/m_{H_i}^2$ and

$$f(\tau) = \begin{cases} \left[\sin^{-1}\left(\sqrt{\frac{1}{\tau}}\right)\right]^2 & \text{if } \tau \geq 1, \\ -\frac{1}{4}\left[\log\left(\frac{\eta_+}{\eta_-}\right) - i\pi\right]^2 & \text{if } \tau < 1, \end{cases} \tag{3.13}$$

---

[1]For the CP-odd scalar H_3^0, there is no dependency on tri-linear scalar couplings as only fermions mediate the loop decay. Therefore the BR for $H_3^0 \rightarrow V\gamma$ is negligible as compared to the one for $H_3^0 \rightarrow ZH/W^\pm H_5^\pm$.

with $\eta_\pm = 1 \pm \sqrt{1-\tau}$. The relevant vertex factors C_{ijk} that enter the calculation of $\Gamma(H, H_5^0 \to \gamma\gamma)$ are as follows:

$$C_{H_3^+ H_3^- H} = \frac{1}{\sqrt{3}v^2}\left[8(\lambda_3 + 3\lambda_4 + \lambda_5)v_\phi^2 v_\chi + 16(6\lambda_2 + \lambda_5)v_\chi^3 + 4M_1 v_\chi^2 - 6M_2 v_\phi^2\right],$$

$$= \frac{1}{\sqrt{3}v^2}\left[\frac{8v_\phi^2 v_\chi}{v_2}(M_{H_5}^2 - M^2 + M_{H_3}^2 + 3\overline{M}^2) + \frac{32v_\chi^3}{v^2}(M_{H_3}^2 + M_{H_5}^2) - \frac{6v_\phi^2 M^2}{12v_\chi}\right],$$

$$C_{H_5^+ H_5^- H} = C_{H_5^{++} H_5^{--} H} = \sqrt{3}\left[8(\lambda_3 + \lambda_4)v_\chi + 2M_2\right]$$

$$= \frac{4\sqrt{3}v_\chi}{v^2}(M_{H_5}^2 - M^2 + M_{H_3}^2 + \overline{M}^2) + \frac{\sqrt{3}M^2}{6v_\chi}, \tag{3.14}$$

$$C_{H_3^+ H_3^- H_5^0} = \sqrt{\frac{2}{3}}\frac{1}{v^2}\left[2(\lambda_3 - 2\lambda_5)v_\phi^2 v_\chi - 8\lambda_5 v_\chi^3 + 4M_1 v_\chi^2 + 3M_2 v_\phi^2\right]$$

$$= \sqrt{\frac{2}{3}}\frac{1}{v^2}\left[4M_{H_3}^2 v_\chi + \frac{16v_\chi^3}{v^2}(M^2 - M_{H_5}^2) + \frac{M^2(v^2 - 8v_\chi^2)}{4v_\chi}\right],$$

$$C_{H_5^+ H_5^- H_5^0} = \sqrt{6}\left(2\lambda_3 v_\chi - M_2\right) = \sqrt{6}\left(2v_\chi\frac{(M_{H_5}^2 - M^2)}{v^2} - \frac{M^2}{12v_\chi}\right),$$

$$C_{H_5^{++} H_5^{--} H_5^0} = -2\sqrt{6}\left(2\lambda_3 v_\chi - M_2\right) = -2\sqrt{6}\left(2v_\chi\frac{(M_{H_5}^2 - M^2)}{v^2} - \frac{M^2}{12v_\chi}\right).$$

In figure 3(a) and figure 3(b) we show the variation of $\Gamma(H_i)/M_i$ for H and H_5^0 respectively for the parameters consistent with all previously mentioned constraints. As evident from the plots, the widths of H and H_5^0 can be huge which is due to the involvement of the tri-linear scalar couplings which contain a term M^2/v_χ. To ensure all the BSM scalars have natural widths we demand $\Gamma(H_i)/M_i < 0.5$ and the resulting points are shown in figure 3(c). Note that $\Gamma(H_i)/M_i$ for the charged scalars and H_3^0 naturally satisfy $\Gamma(H_i)/M_i \ll 1$. It indicates that not all values of v_χ are allowed for all points in the plane of M_{H_5} vs. M_{H_3}. Note that the two-body decays $H \to H_5^{\pm\pm} H_5^{\mp\mp}, H_5^\pm H_5^\mp, H_5^0 H_5^0$ are open for $M_H > 2M_{H_5}$. The region $M_{H_3} > 250\,\text{GeV}$ and $M_{H_5} = [100, 150]\,\text{GeV}$ is not allowed for any value of $v_\chi < 1\,\text{GeV}$ mainly because of such two body decays. There exists a small orange triangular shape starting around $M_{H_5} \sim [100, 140]\,\text{GeV}$ and $M_{H_3} \sim [170, 250]\,\text{GeV}$, where the two body decays are open but nevertheless $\Gamma(H_i)/M_i < 0.5$ is satisfied for $v_\chi > 0.05\,\text{GeV}$. We note that, in this region $M < 50\,\text{GeV}$. Towards smaller M_{H_5}, M_{H_3} all values of v_χ satisfy $\Gamma(H_i)/M_i < 0.5$ as a suitable values of M is available in this region which can regulate the ratio M^2/v_χ. Whereas for $M_{H_5} > 300\,\text{GeV}$ only $M > 100\,\text{GeV}$ is favoured by the previous constraints[2] (mainly perturbative unitarity bound). Therefore, a value of v_χ larger than $0.01\,\text{GeV}$ is required to control the width. Further in this region $\Gamma(H_5^0 \to 2\gamma)/M_{H_5} \propto M_{H_5}^2$ as $M_{H_5} \simeq M$.

3.3 Experimental constraints

Existing experimental constraints come from measurements of the properties of the SM-like Higgs boson, in particular the $h \to \gamma\gamma$ rate and searches for additional scalar states in a variety of channels. Among the BSM Higgs searches, we will consider $H_5^{\pm\pm} \to W^\pm W^\pm$ as well as $H_5^0, H \to \gamma\gamma$. We will not include searches for the pseudoscalar $H_3^0 \to \gamma\gamma$ since this

---

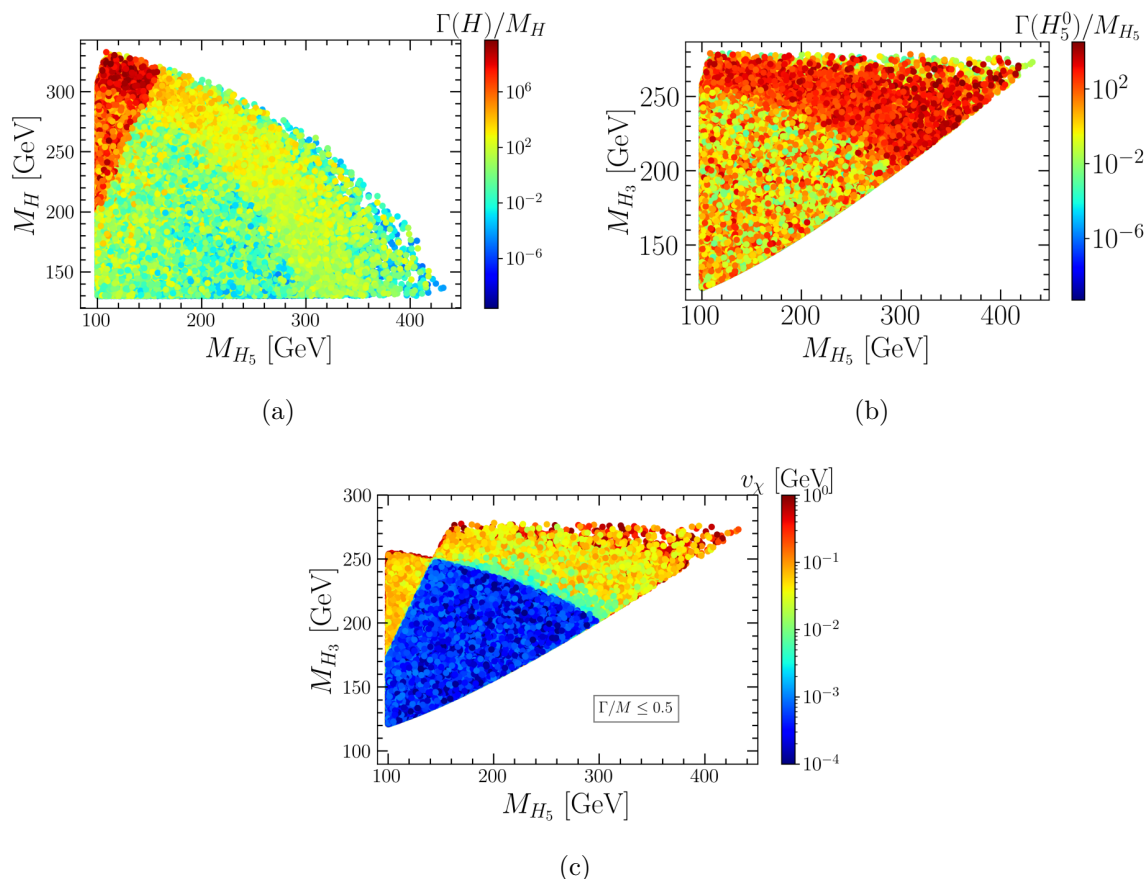[2]The correlation between M and M_{H_5} (M_{H_3}) is shown in figure 9.

Figure 3. Allowed points (a) in the M_{H_5} vs. M_H plane with Γ_H/M_H in the color bar, (b) in the M_{H_5} vs. M_{H_3} plane with Γ_{H_5}/M_{H_5} in the color bar, and (c) in the M_{H_5} vs. M_{H_3} plane with v_χ in the color bar. In the latter, we impose the constraint $\Gamma(H_i)/M_i < 0.5$ for all the scalars. All points satisfy the constraints discussed in sections 3.1 and 3.2.

process does not depend on the tri-linear scalar coupling and, therefore, always features a small branching ratio. The contributions coming from the $t \to H_3^+ b$ and B physics observables like $B_s^0 \to \mu^+\mu^-$, $b \to s\gamma$ are also suppressed because of small v_χ [36] and hence do not provide any constraints on our parameter space. For definiteness note that the experimental constraints discussed below will be applied step-by-step in a cumulative manner to determine the model's final, allowed parameter space.

3.3.1 Higgs-to-diphoton measurements ($h \to \gamma\gamma$)

Higgs-to-diphoton rate is well measured by the ATLAS [40] and CMS [41] searches for $h \to \gamma\gamma$. Charged scalars in this model give rise to additional contributions to $h \to \gamma\gamma$ decay and hence can alter the predicted rate for this channel compared to its SM-predicted value. The signal strength of the SM Higgs for channel $h \to \gamma\gamma$ is given by,

$$\mu_{h\to\gamma\gamma} = \frac{\sigma_h}{\sigma_h^{SM}} \frac{\mathrm{BR}(h \to \gamma\gamma)}{\mathrm{BR}^{\mathrm{SM}}(h \to \gamma\gamma)} \approx \frac{S_{h\gamma\gamma}}{S_{h\gamma\gamma}^{\mathrm{SM}}}, \tag{3.15}$$
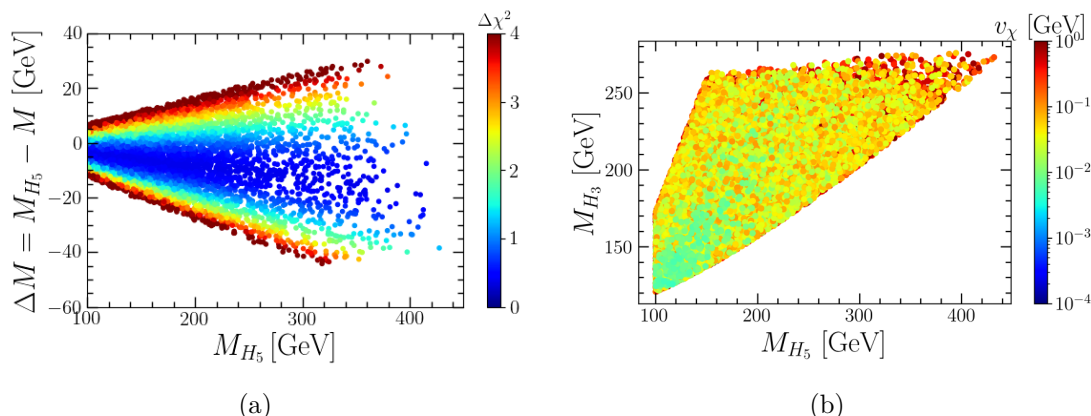
Figure 4. (a) Allowed mass splitting between M_{H_5} and M after imposing the constraint from $h \to \gamma\gamma$ and all theoretical constraints, with $\Delta\chi^2$ shown in color. (b) Allowed points in the M_{H_5} vs. M_{H_3} plane with v_χ in the color bar.

where σ_h and σ_h^{SM} is the production cross section of h through ggF and VBF channel in the GM and SM model respectively. For $v_\chi \leq 1\,\text{GeV}$, the ratio $\sigma_h/\sigma_h^{\text{SM}} \approx 1$. In the above $S_{h\gamma\gamma}$ is defined in eq. (3.10) and the couplings C_{ijk} [17] relevant for $S_{h\gamma\gamma}$ are:

$$C_{H_3^+ H_3^- h} = \frac{c_\alpha}{v^2}\left[(4\lambda_2 - \lambda_5)v_\phi^3 + 8(8\lambda_1 + \lambda_5)v_\phi v_\chi^2 + 4M_1 v_\phi v_\chi\right]$$

$$\simeq \frac{1}{v^2(v^2 - 8v_\chi^2)^{1/2}}\left[2M_{H_3}^2 v^2 + 8v_\chi^2(M_h^2 - 2M_{H_3}^2)\right],$$

$$C_{H_5^+ H_5^- h} = C_{H_5^{++} H_5^{--} h} = (4\lambda_2 + \lambda_5)v_\phi = \frac{2(v^2 - 8v_\chi^2)^{1/2}}{v^2}(M_{H_5}^2 - M^2),$$

$$C_{hW^+W^-} = c_W^2 C_{hZZ} = \frac{(v^2 - 8v_\chi^2)^{1/2}}{2s_W^2}. \tag{3.16}$$

The decay of h to $HH, H_3^+H_3^-, H_5^+H_5^-, H_5^{++}H_5^{--}$ channels is kinematically forbidden for the parameters favoured by the theoretical constraints, so the only decays of h are into SM final states.

We perform a χ^2 analysis to obtain the parameter space consistent with the recent $h \to \gamma\gamma$ signal strength measurement by ATLAS [40] and CMS [41],

$$\mu_{\text{ATLAS}} = 1.04^{+0.1}_{-0.09}, \qquad \mu_{\text{CMS}} = 1.12 \pm 0.09. \tag{3.17}$$

The χ^2 from multiple independent measurements can be computed as,

$$\chi^2 = \sum_i \frac{\mu_i^2 - \hat{\mu}^2}{\sigma_i^+ \sigma_i^- + (\sigma_i^+ - \sigma_i^-)(\mu_i - \hat{\mu})} \tag{3.18}$$

where μ_i and $\sigma_i^\pm$ are the experimental mean values and uncertainties for CMS and ATLAS measurements, and $\hat{\mu}$ is the predicted value. We impose the condition $\Delta\chi^2 = \chi^2 - \chi_{\min}^2 < 4$.

In figure 4(a), we show the allowed points satisfying theoretical, oblique parameter and $h \to \gamma\gamma$ rate constraints in the M_{H_5} vs. ΔM plane where the color bar corresponds to the different values of $\Delta\chi^2$. It is evident from the figure that mass splitting between M_{H_5}
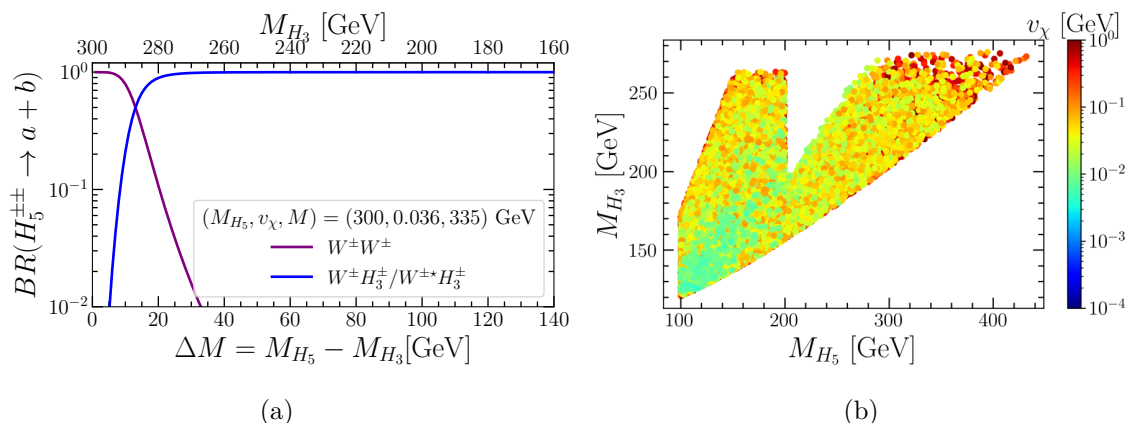
Figure 5. (a) Variation of branching ratios of $H_5^{\pm\pm}$ decays to different channels w.r.t. the mass difference between the fiveplet and triplet states for a specific benchmark point. (b) Allowed points in the M_{H_5} vs. M_{H_3} plane after applying the limit from the ATLAS search for $H_5^{\pm\pm}$ decay to same-sign gauge bosons [42] as well as all previously discussed theoretical constraints, constraints from the measurement of oblique parameters, constraints on the decay width of the BSM scalars, and the measured rate $h \to \gamma\gamma$.

and M cannot be arbitrarily large. The vertex factors $C_{H_5^+ H_5^- h}$ and $C_{H_5^{++} H_5^{--} h}$ depend crucially on ΔM and large values of ΔM will lead to an enhanced diphoton rate and hence in disagreement with the measured rate.

Figure 4(b) shows the variation of v_χ in the M_{H_5} vs. M_{H_3} plane. As can be seen from the figure, the measured diphoton rate discards the points $v_\chi < 4.8 \times 10^{-3}$ GeV. As discussed above M^2/v_χ is restricted due to $\Gamma/M_i < 0.5$. Therefore, lower M is required for lower v_χ. Although $v_\chi \sim 10^{-4}$ GeV satisfy $\Gamma/M_i < 0.5$, the required M for that is so small that the difference between M_{H_5} and M is large and hence the measured $\Gamma(h \to \gamma\gamma)$ rate is disturbed. The combined effect of $\Gamma/M < 0.5$ and $\Gamma(h \to \gamma\gamma)$ rate set lower limit on v_χ.

3.3.2 $H_5^{\pm\pm} \to W^\pm W^\pm$ search

The CMS [43] and ATLAS searches [42, 44] investigated the presence of $H^{\pm\pm}$ decaying into same-sign gauge bosons leading to the multi-lepton final state. In the GM model, the scalar $H_5^{\pm\pm}$ can lead to such signature and hence its production cross section is constrained by the non-observation of such a signal at the LHC. The CMS [43] search targets the production of $H_5^{\pm\pm}$ via vector boson fusion (VBF) channel, however, the $H_5^{++} W^- W^-$ coupling depends on v_χ such that the $H_5^{\pm\pm}$ production rate via VBF for $v_\chi \leq 1$ GeV is suppressed. Hence this CMS search does not set strong limit on our chosen parameter space.

The ATLAS collaboration has searched for pair production of $H_5^{\pm\pm}$ via the Drell-Yan process $pp \to H_5^{\pm\pm} H_5^{\mp\mp}$, which is sensitive to the parameter space considered in our work. The current ATLAS search [42] constrains the doubly charged Higgs mass in the range of 200 GeV to 350 GeV assuming 100% branching ratio for $H_5^{\pm\pm} \to W^\pm W^\pm$. To reinterpret this constraint for our scenario, where the branching ratio of $H^{\pm\pm} \to W^\pm W^\pm$ can vary, we calculate $\sigma(pp \to H_5^{\pm\pm} H_5^{\mp\mp}) \times \mathrm{BR}^2(H_5^{\pm\pm} \to W^\pm W^\pm)$ and compare with the observed limit. Similar multi-leptonic final state can also arise from $pp \to H_5^{\mp\mp} H_5^{\pm\pm}(\to W^\pm H_3^\pm)$

followed by the decay $H_3^\pm \to \ell^\pm \nu$. However, for the range of v_χ that has survived previous constraints, i.e. $v_\chi > 4.8 \times 10^{-3}\,\text{GeV}$, $\text{BR}(H_3^\pm \to \ell^\pm \nu)$ is suppressed and hence this secondary contribution is negligible in our case.

As an understanding of the variation $\text{BR}(H_5^{\pm\pm} \to W^\pm W^\pm)$ is crucial to study the ATLAS limit, in figure 5(a), we present the branching ratio of the $H_5^{\pm\pm}$ of mass $300\,\text{GeV}$ w.r.t. $\Delta M = M_{H_5} - M_{H_3}$ for $M = 335\,\text{GeV}$ and $v_\chi = 0.036\,\text{GeV}$. We choose this benchmark for illustrative purpose, as it corresponds to a point that is allowed by all theoretical and experimental constraints imposed in the following sections. For this value of v_χ, the leptonic decay mode $H_5^{\pm\pm} \to l^\pm l^\pm$ is suppressed[3] and hence only decay channels containing at least one gauge boson are shown. The expressions for the partial decay widths for $H_5^{\pm\pm} \to l^\pm l^\pm, W^\pm W^\pm, H_3^\pm H_3^\pm, W^\pm H_3^\pm / W^{\pm*} H_3^\pm$ are given in appendix A. The partial decay widths $\Gamma(H_5^{\pm\pm} \to W^\pm W^\pm) \sim v_\chi^2$, $\Gamma(H_5^{\pm\pm} \to \ell^\pm \ell^\pm) \sim (Y_\nu/v_\chi)^2$ and $\Gamma(H_5^{\pm\pm} \to W^\pm H_3^\pm)$ are independent of v_χ. Thereby for sufficiently large v_χ the branching ratio $H^{\pm\pm} \to W^\pm W^\pm$ will be significantly large. As can be seen from figure 5(a), for $\Delta M = 0\,\text{GeV}$, the decay $H_5^{\pm\pm} \to W^\pm W^\pm$ is 100%. With the increase of ΔM, M_{H_3} is decreasing thus opening the decay modes $W^{\pm\star} H_3^\pm / W^\pm H_3^\pm$. This channel governs the decay of $H_5^{\pm\pm}$ beyond $\Delta M \sim 30\,\text{GeV}$ for this benchmark point. For the shown mass range, the other decay mode $H_5^{\pm\pm} \to H_3^\pm H_3^\pm$ is not open kinematically. For $\Delta M < M_W$, the decays $H_5^{\pm\pm} \to W^\pm H_3^\pm$ is forbidden, however the decay $H_5^{\pm\pm} \to W^{\pm*} H_3^\pm$ is still open. As we shift towards a smaller mass difference $\Delta M \sim 20\,\text{GeV}$, the branching ratio $\text{BR}(H_5^{\pm\pm} \to W^\pm W^\pm)$ increases, eventually for smaller mass differences $H_5^{\pm\pm} \to W^\pm W^\pm$ becomes the leading decay mode, thereby we expect a strong constraint for a small ΔM. This is clearly evident from figure 5(b), where we show all the points in the M_{H_5} vs. M_{H_3} plane that satisfy theoretical constraints as well as constraints from oblique parameters measurement, from the measured $h \to \gamma\gamma$ rate and from ATLAS same-sign diboson search. The values of v_χ are shown in the color-bar. As expected, the parameter space around $M_{H_5} \sim M_{H_3}$ is ruled out, as in this region $H_5^{\pm\pm} \to W^\pm W^\pm$ has almost 100% branching ratio. Note that there is no constraint from the ATLAS search for $M_{H_5} < 200\,\text{GeV}$, as this range has not been covered in [42].

As stated above, $\text{BR}(H_5^{\pm\pm} \to W^\pm W^\pm)$ depends on M_{H_5}, M_{H_3} and v_χ. In the M_{H_5} vs. M_{H_3} plane, the ATLAS limit will be satisfied when $\text{BR}(H_5^{\pm\pm} \to W^\pm W^\pm)$ is suppressed. This happens in the region where $H_5^{\pm\pm} \to W^\pm H_3^\pm / W^{\pm\star} H_3^\pm$ is open provided v_χ is not too large. Note that for $v_\chi > 4.8 \times 10^{-3}\,\text{GeV}$, $H_5^{\pm\pm} \to \ell^\pm \ell^\pm$ is suppressed and hence $H_5^{\pm\pm}$ dominantly decays to $W^\pm W^\pm$ with $\sim 100\%$ branching ratio. Therefore the region where $\Delta M \to 0$ is excluded by the ATLAS search.

3.3.3 $H_5^0 \to \gamma\gamma$ search

The ATLAS experiment has searched for spin-0 BSM resonances in the diphoton final state using 139/fb data at $\sqrt{s} = 13\,\text{TeV}$ [45]. In our model, the neutral BSM scalars (H_5^0, H) decay to diphoton final states and hence this model can be constrained using this ATLAS diphoton search. In this subsection, we discuss the limit for $H_5^0 \to \gamma\gamma$ and, in the following one, the limit for $H \to \gamma\gamma$.

---

[3]From eq. (2.7), it can be seen that for $v_\chi = 0.1\,\text{GeV}$, we need $Y_\nu \approx 10^{-10}$ to satisfy light neutrino mass. Consequently, the partial decay width for $H_5^{\pm\pm} \to l^\pm l^\pm$ process which is proportional to $(Y_\nu/v_\chi)^2$ is suppressed for small Y_ν.
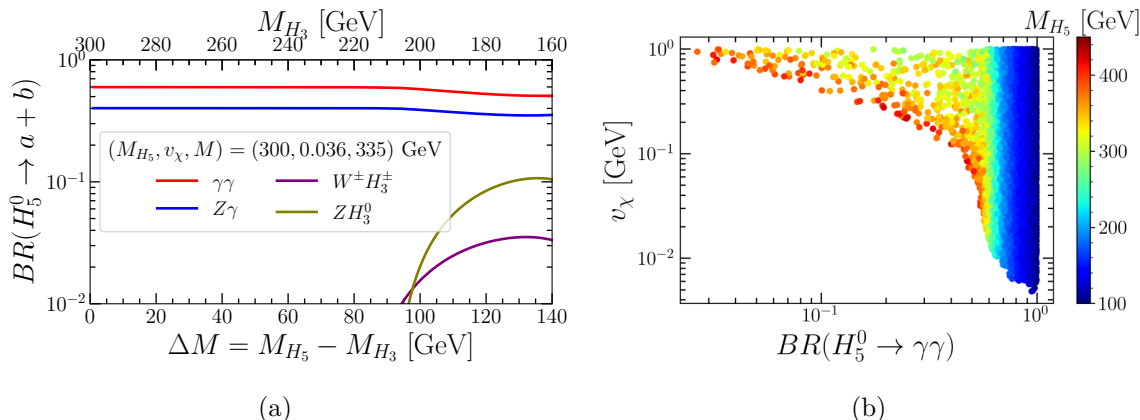
Figure 6. (a) Branching ratio of H_5^0 to different channels for the benchmark point of figure 5(a). (b) Allowed points in the $BR(H_5^0 \rightarrow \gamma\gamma)$ vs v_χ plane consistent with all previous theoretical and experimental constraints.

Before turning to the implementation of the ATLAS analysis, we discuss the variation of $BR(H_5^0 \rightarrow \gamma\gamma)$ in the available parameter space. Among the SM fermions, H_5^0 only interacts with neutrino via Yukawa coupling, which is suppressed unless $v_\chi \lesssim 10^{-4}$ GeV. So, the preferred tree-level decays are $H_5^0 \rightarrow VV, W^\pm H_3^\mp, ZH_3^0$ or $W^{\pm *}H_3^\mp, W^\pm H_3^{\mp *}$ when the two-body tree-level processes are not kinematically open, and among the loop-level decays, $\gamma\gamma$ and $Z\gamma$ are preferred. The partial decay width of $H_5^0 \rightarrow \gamma\gamma$ can be calculated following eq. (3.9) for $H_i = H_5^0$. The relevant vertex factors that enter the calculation of $\Gamma(H_5^0 \rightarrow \gamma\gamma)$ are as follows:

$$
\begin{aligned}
C_{H_3^+ H_3^- H_5^0} &= \sqrt{\frac{2}{3}} \frac{1}{v^2} \left[2(\lambda_3 - 2\lambda_5)v_\phi^2 v_\chi - 8\lambda_5 v_\chi^3 + 4M_1 v_\chi^2 + 3M_2 v_\phi^2 \right] \\
&= \sqrt{\frac{2}{3}} \frac{1}{v^2} \left[4M_{H_3}^2 v_\chi + \frac{16 v_\chi^3}{v^2}(M^2 - M_{H_5}^2) + \frac{M^2(v^2 - 8v_\chi^2)}{4v_\chi} \right], \\
C_{H_5^+ H_5^- H_5^0} &= \sqrt{6} \left(2\lambda_3 v_\chi - M_2 \right) = \sqrt{6} \left(2v_\chi \frac{(M_{H_5}^2 - M^2)}{v^2} - \frac{M^2}{12v_\chi} \right), \\
C_{H_5^{++} H_5^{--} H_5^0} &= -2\sqrt{6} \left(2\lambda_3 v_\chi - M_2 \right) = -2\sqrt{6} \left(2v_\chi \frac{(M_{H_5}^2 - M^2)}{v^2} - \frac{M^2}{12v_\chi} \right), \\
C_{H_5^0 W^+ W^-} &= \sqrt{\frac{2}{3}} \frac{1}{s_W^2} v_\chi \,.
\end{aligned}
\tag{3.19}
$$

Note in particular that the contributions from the W bosons are suppressed while the charged Higgses contributions can be strongly enhanced for small v_χ due to the presence of M^2/v_χ in the respective vertex factors. As a result, the partial decay widths of both $H_5^0 \rightarrow \gamma\gamma$ and $H_5^0 \rightarrow \gamma Z$ are inversely proportional to v_χ^2. Hence, for a small v_χ, the branching ratio for $H_5^0 \rightarrow \gamma\gamma, Z\gamma$ can be significantly enhanced. We provide the analytic expressions for the partial decay widths for all final states in appendix A and in eq. (3.9). For the numerical analysis, we have implemented the model in microMEGAs6.0 [46] using Feynrules [47] and we use the code to compute all tree-level and loop-induced decays of the scalars. When there are no tree-level two-body processes we also include 3-body processes. In figure 6(a),
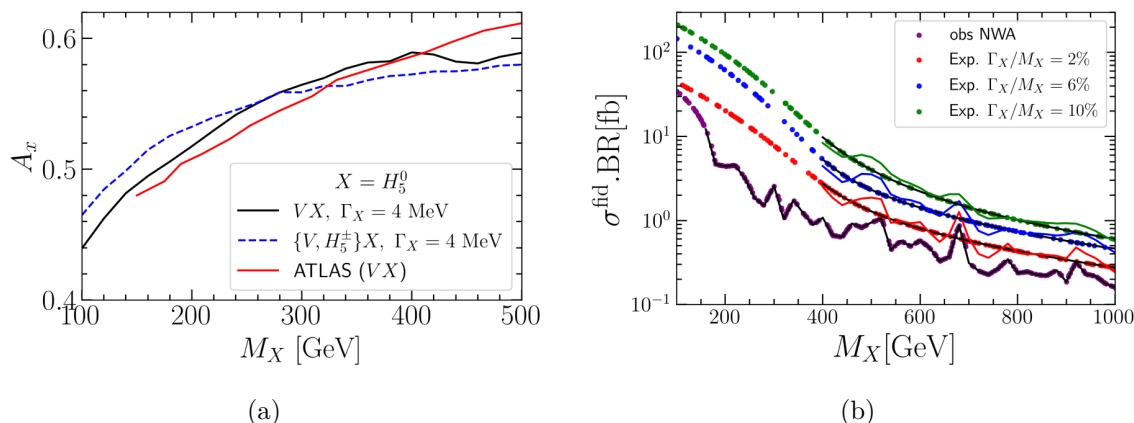
Figure 7. (a) Efficiency for diphoton selection cuts as a function of the mass M_X of the diphoton resonance, following the search $X \to \gamma\gamma$ [45]. (b) Observed and expected limit on the diphoton cross section.

we show the variation of the relevant branching ratios for our chosen benchmark point. As expected, for smaller v_χ, H_5^0 dominantly decays to loop-induced processes, such as, $\gamma\gamma$ and γZ. Thus the BSM resonance search decaying into diphotons final state at the LHC can constrain the model significantly.

In figure 6(b), we show the dependency of $\mathrm{BR}(H_5^0 \to \gamma\gamma)$ on the vev v_χ and the mass of the fiveplet M_{H_5}, for all the points that satisfy the previously mentioned constraints. Note that since the theory constraints require $M_{H_5} < \sqrt{3}M_{H_3}$, the decay mode $H_5^0 \to H_3^\pm H_3^\mp$ is kinematically forbidden. The figure indicates that for a smaller $v_\chi < \mathcal{O}(0.1)\,\mathrm{GeV}$ and for the specified variation of the parameter M, the branching ratio of $H_5^0 \to \gamma\gamma$ is always larger than 40% irrespective of the M_{H_5} value. Since over a large range of parameters, BSM Higgs decaying into diphoton has a significantly large branching ratio, hence we expect to receive tight constraint from ATLAS diphoton resonance search $X \to \gamma\gamma$ [45]. Following this ATLAS search, we implement the following set of cuts on our signal sample. In the ATLAS search, for the associate production mode, the experimental collaboration considered $pp \to VX$ process, where V is $W^\pm/Z$. In our case, our main production mode is somewhat different $pp \to H_5^0 H_5^\pm$, which will lead to a different cut-efficiency. Hence, we first validate our selection cuts with the same sample that have been considered in the ATLAS search, and later calculate the final cut-efficiency taking into account the relevant channels.

Acceptance cuts:

- c_1: number of photons $N^\gamma \geq 2$,

- c_2: $c_1 + \{p_T^{\gamma_{1,2}} \geq 25\,\mathrm{GeV},\ |\eta^{\gamma_{1,2}}| < 2.37,\ \mathrm{isolation}^4\ \mathrm{for}\ \gamma_{1,2}\ \}$

- c_3: $c_2 + \{\ \mathrm{Reject\ event\ with}\ 1.37 < |\eta^{\gamma_{1,2}}| < 1.52\ \}$

- c_4: $c_3 + \{p_T^{\gamma_1}/M(\gamma_1\gamma_2) > 0.3,\ p_T^{\gamma_2}/M(\gamma_1\gamma_2) > 0.25\ \}$, where $M(\gamma_1\gamma_2)$ is the invariant mass of the two leading photons.

---

[4]For isolation we demand scalar sum of p_T of all the stable particles (except neutrinos) found within a $\Delta R = 0.4$ cone around the photon direction, is required to be less than $0.05\,p_T + 6\,\mathrm{GeV}$.

	$M_X \geq 400\,\mathrm{GeV}$	$M_X < 400\,\mathrm{GeV}$
$6\% < \Gamma_X/M_X$	10% obs. limit	10% extrapolated exp. limit
$2\% < \Gamma_X/M_X \leq 6\%$	6% obs. limit	6% extrapolated exp. limit
$1\% < \Gamma_X/M_X \leq 2\%$	2% obs. limit	2% extrapolated exp. limit
$\Gamma_X/M_X \leq 1\%$	NWA obs. limit	NWA obs. limit

Table 2. Selection of the ATLAS limit depending on the mass and decay width of the diphoton resonance.

In figure 7(a), we show the efficiency (A_x) for diphoton selection cuts w.r.t. the mass of the diphoton resonance M_X ($X = H_5^0$). The red line is extracted from the ATLAS analysis for associated production with a vector boson $pp \to VX$ and for a total width $\Gamma = 4\,\mathrm{MeV}$. The black line corresponds to $pp \to VH_5^0(\to 2\gamma)$ for $\Gamma(H_5^0) = 4\,\mathrm{MeV}$, which we compute. The efficiency for the mode $\{V, H_5^\pm\}X$ is shown by the blue-dashed line assuming $\Gamma(H_5^0) = 4\,\mathrm{MeV}$. The efficiency for this mode is different than that for VX for two reasons. First, the photon p_T for $\{V, H_5^\pm\}X$ is larger than that for VX. This occurs because larger momentum of H_5^0 for $\{V, H_5^\pm\}X$ than VX. Another reason for the difference in A_x between the two processes is coming from the isolation requirement of two photons. For the process VX, from $W^\pm/Z$ there are one lepton/jet pair, which can fall within a $\Delta R = 0.4$ cone around the photon direction. For $\{V, H_5^\pm\}X$, $H_5^\pm \to W^\pm Z$ with subsequent decay of the gauge bosons to leptons/jet pairs, there are more number of particles in the final state. Hence demanding the same isolation criterion somewhat reduces the cut-efficiency. We note that H_5^0 can also be produced in association with $H_3^\pm, H_3^0$ via $pp \to H_5^0\{H_3^\pm, H_3^0\}$. For this channel A_x depends on M_{H_3} as well. However, contribution of this channel to the total production rate of H_5^0 is less than 10%. Hence, there is no notable variation of efficiency with M_{H_3}. Further, H_5^0 can be pair produced via off shell Higgs, $pp \to h \to H_5^0 H_5^0$ but this cross section is suppressed compared to other channels. We do not include these sub-dominant channels while calculating the cut efficiency but for the production cross section we consider contribution of all possible channels.

In figure 7(b), we show the expected and observed upper limits at 95% CL on the fiducial cross-section times branching ratio to two photons for a spin-0 resonance as a function of its mass M_X for different values of $\Gamma_X/M_X = (10, 6, 2)\%$ [45]. The expected limits are shown by black solid lines and the observed limits by the coloured solid lines. The observed limit varies w.r.t. the width of the diphoton resonance, being much weaker for higher values of Γ_X/M_X. For $\Gamma_X/M_X = (10, 6, 2)\%$, the observed limit for a mass lighter than $400\,\mathrm{GeV}$ is not given in the ATLAS paper [45], thus we extrapolate the corresponding expected limit and consider that as observed limit. The various coloured circle upto $M_X = 400\,\mathrm{GeV}$ indicates extrapolated data of the expected limits for $\Gamma_X/M_X = (10, 6, 2)\%$. The purple points indicate the interpolated data of the observed upper limits at 95% CL for the narrow width approximation (NWA) and the black line under purple points is the corresponding ATLAS data. If $\Gamma_X/M_X \leq 1\%$ we consider the NWA limit, else we follow table 2.

Figure 8(a) shows the parameter space in the M_{H_5} vs. M_{H_3} plane that passes the diphoton limit for $H_5^0 \to 2\gamma$. We calculate the fiducial production cross-section times branching ratio to diphoton mode for H_5^0 and compare with the observed 95% CL limit by the ATLAS search.
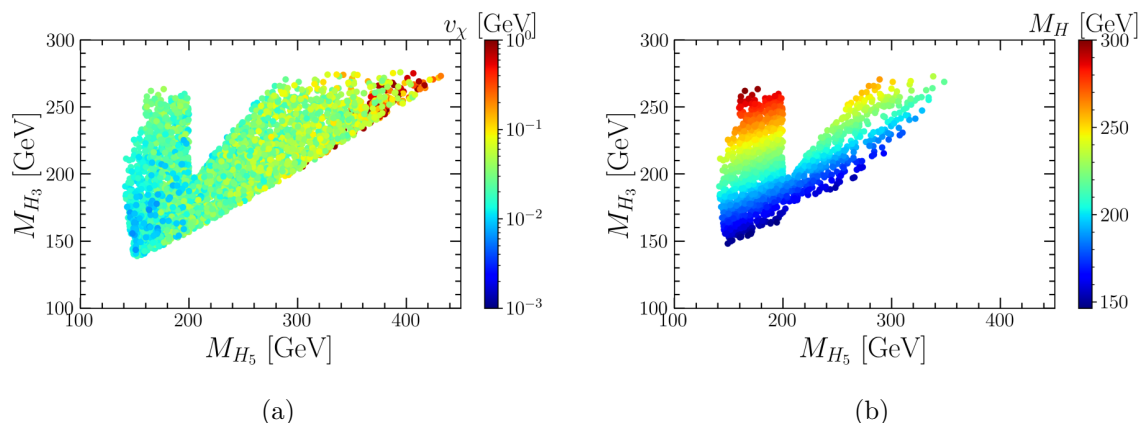
Figure 8. (a) Allowed points after imposing the limit on $H_5^0 \to \gamma\gamma$ with v_χ in the color bar. (b) Allowed points after imposing in addition the limit on $H \to \gamma\gamma$ with M_H in the color bar.

The leading production channel is $pp \to H_5^0 H_5^\pm$ which depends mostly on M_{H_5} while the BR($H_5^0 \to 2\gamma$) depends on M_{H_5}, M_{H_3}, and M^2/v_χ. We note that, $pp \to H_5^0 H_5^0$ mode has a very small cross-section and therefore does not have any large impact. If $H_5^0 \to VV/VH_3^{0/\pm}$ is either kinematically closed, or suppressed due to a small v_χ, the leading decay modes are $H_5^0 \to 2\gamma/Z\gamma$ which depends on M^2/v_χ. Note that M is already constrained by the SM Higgs diphoton rate and the allowed value of M is $\mathcal{O}(100)\,\text{GeV}$. For the values of M^2/v_χ favoured by the previous bounds, $H_5^0 \to VV$ mode is suppressed. The total width is determined by the $H_5^0 \to 2\gamma/Z\gamma$ modes which varies as $\sim 1/v_\chi^2$, as also has been emphasized before. As the observed limit on the cross section is stronger for a narrow resonance (see figure 7(b)), larger v_χ for which H_5^0 has smaller width is excluded. Contrary to that, lower v_χ passes the ATLAS limit for which the width of H_5^0 is larger and has a weaker limit. We find that $v_\chi \sim \mathcal{O}(1)\,\text{GeV}$ is significantly constrained over a large mass range, except $300\,\text{GeV} < M_{H_5} < 400\,\text{GeV}$, represented by the red points.

3.3.4 $H \to \gamma\gamma$ search

We perform a similar analysis for the singlet scalar in the channel $H \to 2\gamma$. The dominant production channels for H is $pp \to HH_3^{\pm,0}$ and the main decays are to $2\gamma/Z\gamma$ via loop. The corresponding vertex factor is proportional to M^2/v_χ. The decay $H \to W^\pm W^\mp$ is suppressed by kinematics and/or because the coupling depends on v_χ, which is $\leq 1\,\text{GeV}$, see eq. (A.4). We obtain the fiducial cross section after calculating the cut efficiency (A_x) with the same set of cuts as mentioned for the case of H_5^0. Note that A_x for this channel varies between 0.5 to 0.59, depending on M_H and M_{H_3}. To check the diphoton limit, we compare the fiducial cross section for this model with the observed limit in a similar way as for H_5^0. Figure 8(b) shows allowed values of M_{H_5}, M_{H_3} and M_H that pass the diphoton limit for $H \to 2\gamma$. In figure 9, we show the allowed parameter space by orange colour, which is consistent with $H \to 2\gamma$ limit as well as all previously discussed constraints. We consider all possible planes such as M_{H_5} vs. M, M_{H_5} vs. v_χ. From figure 9, it is evident that the points with $v_\chi > 0.05\,\text{GeV}$ are mostly excluded because the width of H becomes very narrow, $\Gamma/M_H \lesssim 2\%$, which corresponds to the stronger limit on the observed cross-section as can be seen from figure 7(b). For
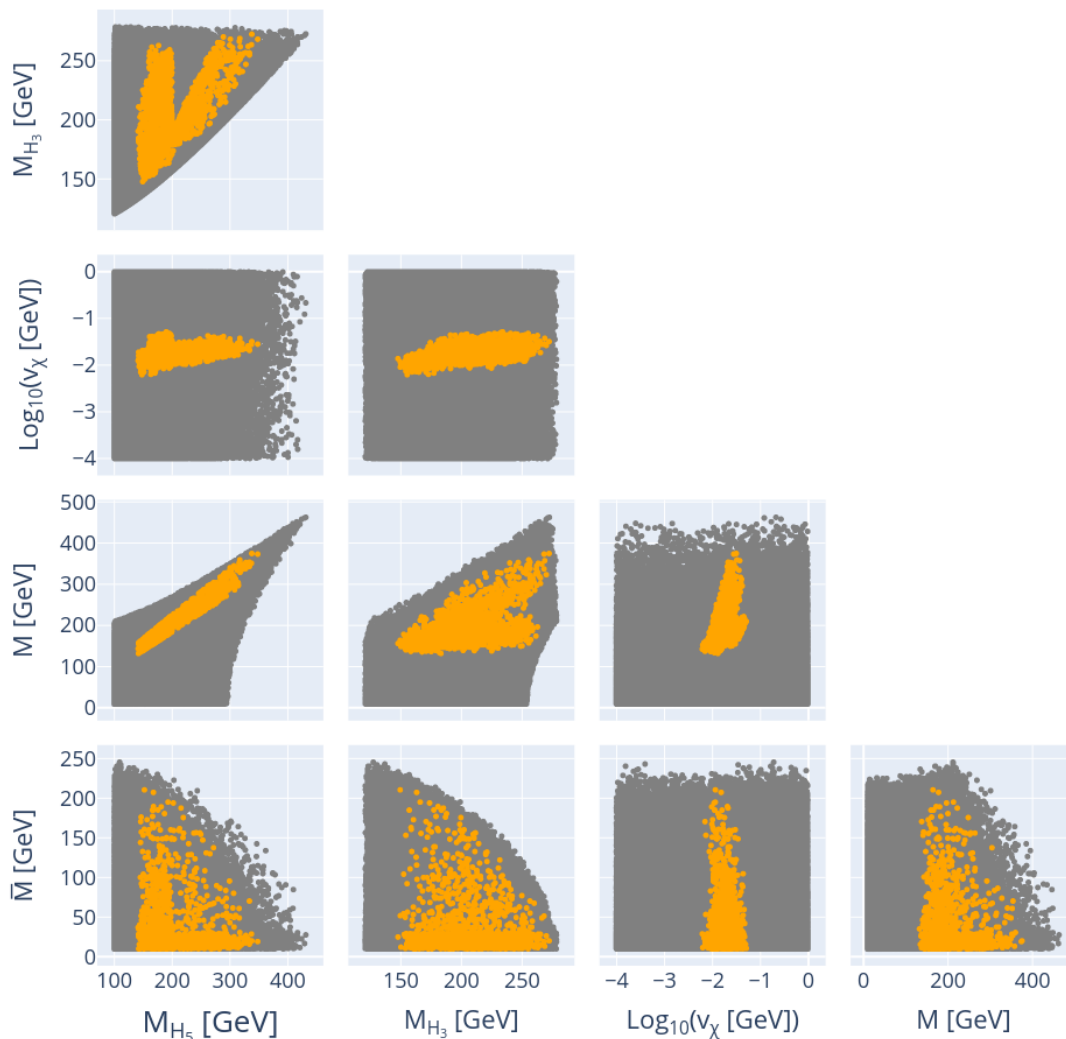
Figure 9. Allowed parameter space after theoretical constraints (grey points) and experimental constraints from colliders (orange points) have been imposed.

$v_\chi \leq 0.05$ GeV, the width Γ/M_H becomes large $\Gamma/M_H \sim \mathcal{O}(6-50)\%$ and the experimental constraint weakens significantly. Therefore only points where $v_\chi \leq 0.05$ GeV are allowed. Finally when v_χ is even smaller then Γ/M_H becomes very large, we have excluded those points by the condition on the total width. We conclude this section with the observation that after taking into account diphoton limit for H, the five-plet mass M_{H_5} becomes more constrained $M_{H_5} < 350$ GeV, while the allowed value of M_H is in between 145 GeV and 300 GeV; M_{H_3} can vary in between 150 GeV and 270 GeV, and the vev $v_\chi \leq 0.05$ GeV. Improvement in the di-photon signal sensitivity by 3 to 4 order of magnitude by future LHC search can probe the complete range of $v_\chi = [10^{-4}, 1]$ GeV. Furthermore, as the $H_5^{\pm\pm} \to W^\pm W^\pm$ search sets an upper bound on v_χ, tighter limits on same-sign gauge boson production can also shrink the range of v_χ. To improve the constraint on v_χ for $M_{H_5} < 200$ GeV, however, one would need to extend the $H_5^{\pm\pm} \to W^\pm W^\pm$ search to the low mass region where $H_5^{\pm\pm} \to W^\pm W^{\pm\star}$ is open.

	Total number of points sampled	4×10^6
	Constraints	**Number of points survived**
c1:	Theory	418410
c2:	c1 + Oblique parameters	418239
c3:	c2 + $\Gamma/M < 0.5$	307117
c4:	c3 + $h \to \gamma\gamma$ measurements	18476
c5:	c4 + $H_5^{++/--} \to W^{\pm}W^{\pm}$ measurements	16491
c6:	c5 + $H_5^0 \to \gamma\gamma$ measurements	3447
c7:	c6 + $H \to \gamma\gamma$ measurements	1446

Table 3. Total number of points that satisfy different constraints.

4 Dark matter observables

4.1 The scalar singlet as cold dark matter

As mentioned before, in our discussions of the GM-S model the singlet scalar S serves as the WIMP DM candidate due to the Z_2 symmetry which makes it stable. The observed relic density of DM is obtained through the pair annihilation of S to bath particles in the early universe. The evolution of the number density of DM, n_S, in the early Universe is governed by the Boltzmann equation, which reads [48],

$$\frac{dn_S}{dt} + 3\mathrm{H}n_S = -\langle \sigma v \rangle (n_S^2 - n_S^{\mathrm{eq}2}), \tag{4.1}$$

where n_S^{eq} is the equilibrium number density of S, $\langle \sigma v \rangle$ is the thermal average cross section for the annihilating DM particles and H is the Hubble parameter. The Boltzmann equation can be written in terms of the co-moving number density, $Y_S = n_S/s$, where s is the entropy number density of the Universe,

$$\frac{dY_S}{dx} = -\frac{s(T)}{H(T)x}\langle \sigma v \rangle (Y_S^2 - Y_S^{\mathrm{eq}2}), \tag{4.2}$$

where $x = m_S/T$ and the Hubble parameter and entropy density [48, 49],

$$H(T) = \frac{\pi}{\sqrt{90}}\frac{\sqrt{g_{\mathrm{eff}}(T)}}{M_{pl}}T^2, \quad s(T) = h_{\mathrm{eff}}(T)\frac{2\pi^2}{45}T^3. \tag{4.3}$$

Here, g_{eff}, h_{eff} are the effective degrees of freedom for the energy and entropy densities of the Universe at temperature T, Y_S^{eq} is the value of Y_S when $n_S = n_S^{\mathrm{eq}}$, [48] and is given by:

$$Y_S^{eq} = \frac{45g}{4\pi^4}\frac{x^2 K_2(x)}{h_{\mathrm{eff}}(T)}. \tag{4.4}$$

In the above, the internal degree of freedom g takes value unity for the case of S which is a real scalar field. Solving eq. (4.2), the DM relic density can be obtained using the relation [50]

$$\Omega_S h^2 = 2.755 \times 10^8 \left(\frac{M_S}{\mathrm{GeV}}\right) Y_S(\mathrm{T_{now}}), \tag{4.5}$$

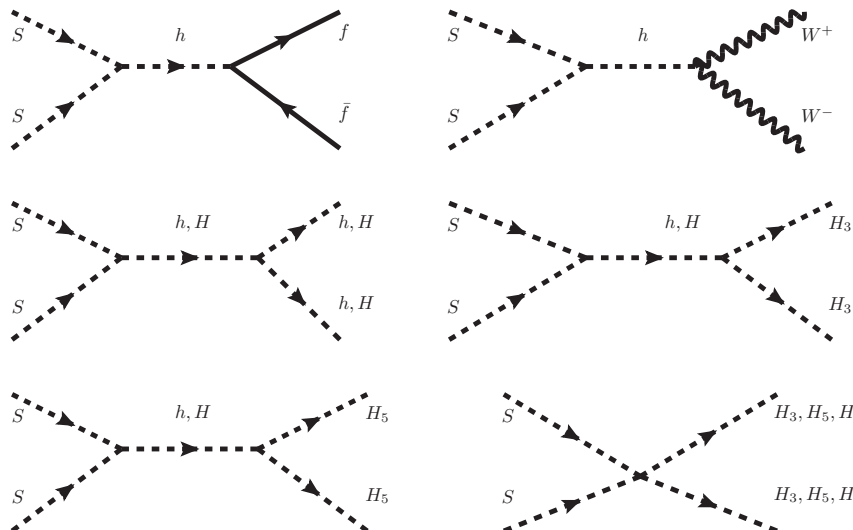where h is the reduced Hubble constant.

Figure 10. Tree level Feynman diagrams for DM pair annihilation into SM/BSM particles where we use notation $H_3 = H_3^0, H_3^+$ and $H_5 = H_5^0, H_5^+, H_5^{++}$.

Vertex	Vertex Factor
SSh	$-4\lambda_a v_\phi$
SSH	$-4\lambda_b v_\chi$
$SShh$	$-4\lambda_a$
$SSHH$	$-4\lambda_b$
SSH_3H_3	$-4(\lambda_b c_H^2 + \lambda_a s_H^2)$
SSH_5H_5	$-4\lambda_b$

Table 4. Couplings of DM with SM and BSM scalars where we use the notation $H_3 = H_3^0, H_3^+$ and $H_5 = H_5^0, H_5^+, H_5^{++}$.

The precise determination of the observed relic density of DM has been achieved through PLANCK measurements of the cosmic microwave background (CMB) [51],

$$\Omega h^2 = 0.120 \pm 0.0012 \tag{4.6}$$

All possible S pair annihilation channels that can contribute to $\langle \sigma v \rangle$ in eq. (4.2) are shown in figure 10. The $SS \to \text{SM} + \text{SM}$ annihilation channels depend only on λ_a, the coupling of the singlet to the Higgs, see table 4. These channels are the same ones that contribute to DM annihilation in the real singlet scalar model [28, 52, 53]. In the GM-S model additional channels, such as $SS \to H_3H_3, H_5H_5, HH$ contribute to DM annihilation. All the couplings involving the BSM scalars depend on λ_b, see table 4. The two couplings λ_a and λ_b are therefore the only parameters that govern the DM phenomenology in addition to the mass parameters. Other than the quartic interaction governing $SS \to H_3H_3, H_5H_5, HH$, s-channel mediated process $SS \to H \to H_5H_5, H_3H_3$ can also give large contribution to the annihilation cross-section, if kinematically accessible. This is a result of the enhancement of couplings HH_5H_5 and HH_3H_3, for small values of v_χ, which can be seen from eq. (3.14).
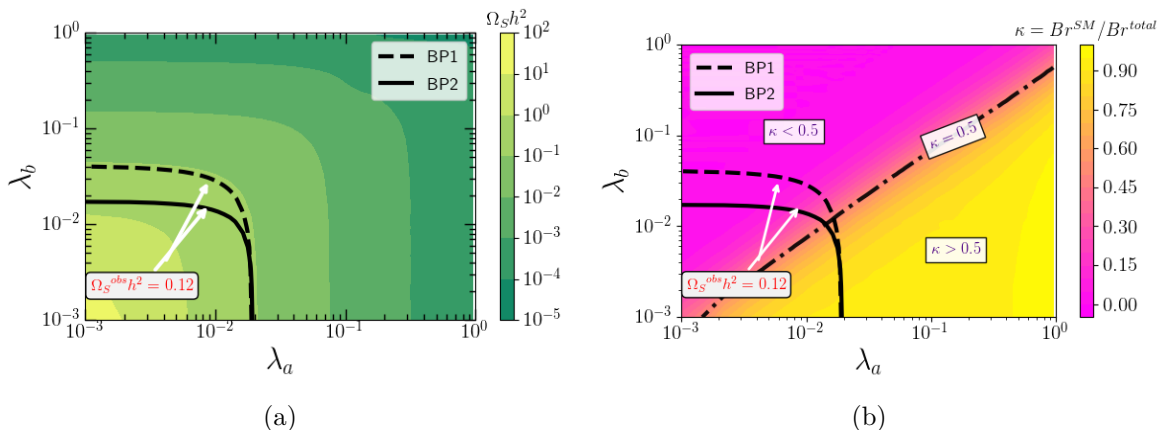
Figure 11. (a) Contours of $\Omega_S h^2$ in the plane of λ_b vs. λ_a for BP1. The black dashed and solid lines superimposed on these indicate the contour corresponding to $\Omega_S h^2 = 0.12$ for BP1 (BP2). (b) Contours of κ, the ratio of DM annihilation to SM vs. (SM+BSM) particles, in the λ_b vs. λ_a plane again for BP1. The dot-dashed line corresponds to scenarios where DM annihilates equally to SM and BSM particles. The black dashed and solid lines superimposed on these indicate the contour corresponding to $\Omega_S h^2 = 0.12$ for BP1 (BP2).

We will first consider only two benchmark points to illustrate the impact of various DM constraints on the parameters relevant for the discussion of DM, viz. λ_a, λ_b and M_S, leaving a complete exploration of the entire allowed parameter space of the model to section 4.3. Recall from the discussions in section 4.3 and section 3, that the current theoretical and experimental constraints restrict the mass of the new scalars in a relatively narrow range, namely 140 GeV $< M_{H_5} < 350$ GeV, 150 GeV $< M_{H_3} < 270$ GeV and 145 GeV $< M_H < 300$ GeV. For our two benchmark points, we fix the value of M_S at 280 GeV and choose the other masses so as to cover the range of allowed masses for M_{H_5}, M_{H_3} and M_H mentioned above. The two benchmark points are thus defined as

- BP1: $M_{H_5} = 300$ GeV, $M_{H_3} = 254$ GeV, $M_H = 227$ GeV, $v_\chi = 0.036$ GeV, $M = 335$ GeV, $\overline{M} = 43$ GeV and $M_S = 280$ GeV

- BP2: $M_{H_5} = 190$ GeV, $M_{H_3} = 234$ GeV, $M_H = 253$ GeV, $v_\chi = 0.05$ GeV, $M = 210$ GeV, $\overline{M} = 10$ GeV and $M_S = 280$ GeV

We use micrOMEGAs6.0 [46] to obtain the DM relic density according to eq. (4.5). To that end, we generate the necessary CalcHEP [54, 55] files using Feynrules [47]. In figure 11(a), we show contours of relic density $\Omega_S h^2 = 0.12$ in the λ_a vs. λ_b plane for the two benchmarks BP1 and BP2. These are superimposed on the contours in shades of green of $\Omega_S h^2$ for BP1. The ones for BP2 are qualitatively similar. As expected for a typical WIMP candidate, $\Omega_S h^2$ decreases when the values of the coupling of the DM to SM (λ_a) and/or to new scalars (λ_b) increase. The overabundant region corresponds to small values of both λ_a and λ_b. When λ_b is below $\approx 10^{-2}$, annihilation into SM final states dominates and the relic density is the same for the two benchmarks since they both feature the same DM mass. When λ_a drops below $\approx 10^{-2}$, annihilation into custodial multiplets dominates. The value of λ_b corresponding to $\Omega_S h^2 = 0.12$ is larger for BP1 than for BP2 because for BP1 the final state $H_5 H_5$ is not
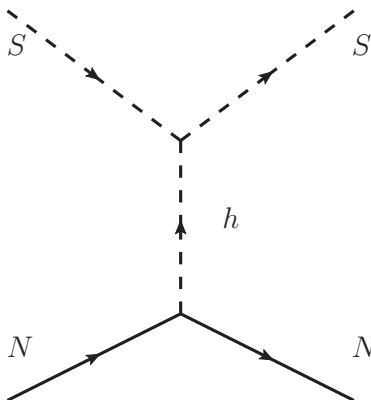
Figure 12. Feynman diagram for the elastic scattering of DM S on nucleons N via Higgs exchange.

kinematically accessible. The value of κ, representing the ratio of DM annihilation to SM vs. (SM+BSM) particles is illustrated in figure 11(b), again for BP1. Superimposed on it are the contours of $\Omega_S h^2 = 0.12$ for BP1 and BP2, indicated by the dashed and solid black curve. For $\lambda_a \approx \lambda_b$, DM annihilates equally to SM and custodial multiplets as shown by the dashed line corresponding to $\kappa = 0.5$. The behaviour of κ for BP2 is also qualitatively similar to that for BP1. It is essential to highlight that $\sin\alpha$ is identically zero in this analysis, for $\lambda_a > \lambda_b$, the GM-S model mimics the behaviour of the real singlet scalar DM extension of SM.

4.2 Direct and indirect detection

Direct searches for DM through its scattering on nuclei pose severe constraints on WIMP DM models. In the GM-S model, the elastic scattering of the DM S on nucleons occurs via t-channel Higgs exchange as shown in figure 12. In the decoupling limit where $\sin\alpha = 0$, there is no tree-level contribution from the t-channel exchange of the BSM Higgs bosons H. The spin independent cross section, σ_{SI}, for the process $SN \to SN$ where N is a nucleon is given by

$$\sigma_{SI} = \frac{4}{\pi}\mu_r |A^{SI}|^2 \,, \tag{4.7}$$

where $\mu_r = \frac{M_S M_N}{M_S + M_N}$ with M_N the nucleon mass and A^{SI} is the nucleon amplitude which depends on the DM interaction with nucleons and the nucleon form factors. To evaluate the spin independent cross section we use micrOMEGAs6.0 [46]. For the two benchmark points, we compare the predicted cross section with the current experimental data from LUX-Zeplin(LZ) [56]. We also examine the future reach of XENONnT [57] and DARWIN [58].

In figures 13(a) and 13(b) we show how the relative contributions to the DM pair annihilation into the channels SM SM, $H_3 H_3$, $H_5 H_5$ and HH vary with λ_a for BP1 and BP2 respectively. For each benchmark point, the value of λ_b is fixed to the value that leads to the observed relic density. In both cases, we observe that for $\lambda_a > 10^{-2}$, the dominant contributions arise from DM annihilation into the SM states. However, this region is stringently constrained from current direct detection data from PANDAX-4T, Xenon1T and particularly LZ. The current limit from LZ sets an upper limit on $\lambda_a \sim 0.007$ (0.005) for BP1(BP2). In the future, this upper limit can be lowered to $\lambda_a \sim 1.5 \times 10^{-3}$ with XENONnT and to $\lambda_a \sim 5.5 \times 10^{-4}$ with DARWIN [58]. For values of λ_a below the current
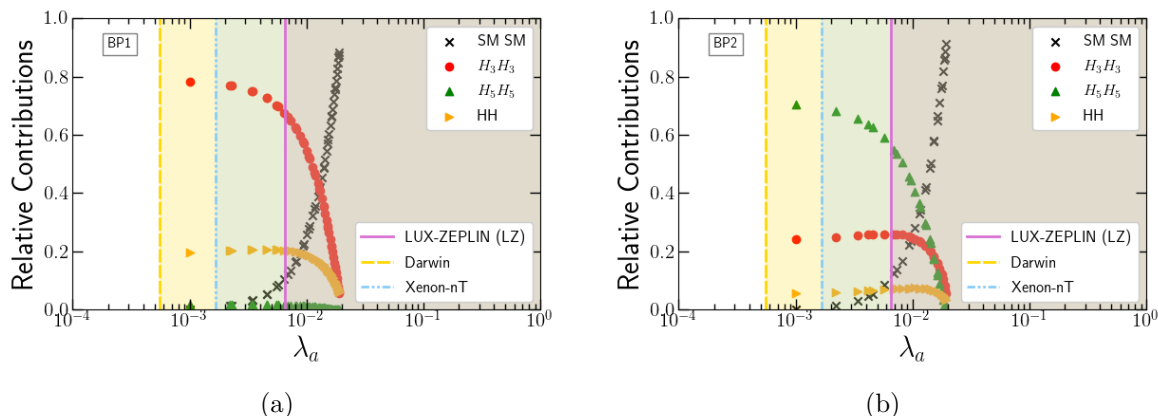
Figure 13. Relative contribution of DM pair annihilation into various final states vs λ_a for benchmark points (a) BP1 and (b) BP2. The direct detection limits on λ_a from Lux-Zeplin (LZ) [56] as well as future projections from DARWIN [58] and XENONnT [57] are also displayed. Note that all the points satisfy the observed DM relic density.

LZ limit, the non-SM modes dominate over the SM, channels with $H_3 H_3$ being the dominant mode for BP1 and $H_5 H_5$ for BP2.

Dark matter can also be detected indirectly by observing gamma rays originating from DM annihilation in galaxies. In particular, DM annihilates to SM and BSM final states via s-channel process mediated by the Higgses and via quartic interactions as shown in figure 10. The photon spectra originating from all final states are computed with micrOMEGAs and we use [59] to determine the indirect constraints extracted from Dwarf Spheroidal Galaxies from the Fermi-LAT and MAGIC telescopes [60, 61]. We use [62] as implemented in micrOMEGAs 6.1 to compare the photon spectra with the expected sensitivity of CTA.

Figure 14 shows the associated photon energy spectra for different values of λ_b for BP1 and BP2 satisfying the relic density constraint. For both benchmarks, there is a kinematic edge at $E \sim 227\,\text{GeV}$ which follows from the fact that the dominant channel which leads to photon final states is HH and $H_5 H_5$ for BP1 and BP2 respectively as can be seen in figure 15. For the larger value of λ_b, annihilation into BSM states dominates over SM annihilation channels. This then leads to more high-energy photons above 100 GeV. The gamma-ray flux of high-energy photons from 100 GeV to 100 TeV originating from the DM pair-annihilation results in better sensitivity in CTA [63, 64]. Thus, for both BP1 and BP2, CTA sensitivity increases due to the hard photon spectrum, resulting in probing the $\langle \sigma v \rangle$ well below the typical WIMP DM annihilation $\langle \sigma v \rangle \sim 3 \times 10^{-26}\,\text{cm}^3\text{sec}^{-1}$. Figures 14(c) and 14(d) show variation of $\langle \sigma v \rangle$ varies with λ_b. The limits from indirect detection searches from Fermi-LAT and the projected reach of CTA at 95% CL (following ref. [62]) are shown as well. As can be seen, the direct detection (DD) experiments severely constrain the lower values of λ_b. The red points in figures 14(c) and 14(d) represent the points allowed both by DD and Fermi-LAT, although we notice that Fermi-LAT constraints do not impose any stringent restrictions for our parameter space. In blue dashed line, we show the future projection for indirect detection searches with CTA. As can be seen, CTA will have the sensitivity to probe both benchmark points for any value of λ_b.
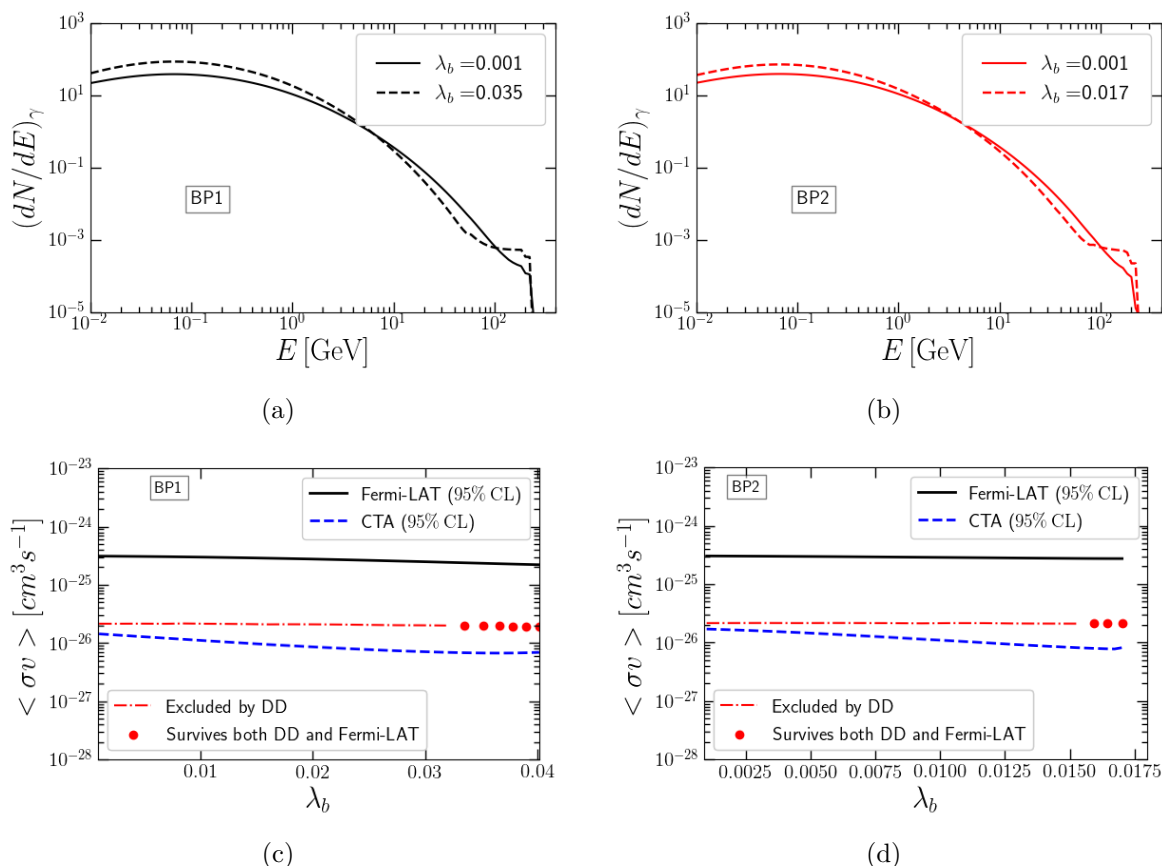
Figure 14. Upper row: photon spectrum for two different choices of λ_b for (a) BP1 and (b) BP2. Lower row: theoretical prediction for $\langle \sigma v \rangle$ vs. λ_b for (c) BP1 and (d) BP2. The dash-dot line shows the region excluded by LZ. The current limit from FermiLAT (full) and the sensitivity of CTA (dash) are also shown. Note that all the points satisfy the observed DM relic density.

Figures 15(a) and 15(c) show the relative contributions of DM annihilation channels versus M_S. Dark matter masses below 200 GeV are severely constrained from direct detection searches. For BP1, the dominant channel always corresponds to the heavier state that is kinematically accessible: viz. $H_3 H_3$ for $M_S \sim 280$ GeV and $H_5 H_5$ for $M_S \sim 300$ GeV. For BP2, $H_5 H_5$ is the dominant channel followed by subdominant contributions from $H_3 H_3$, HH and $SMSM$ for the entire mass range for $M_S > 200$ GeV. The annihilation cross-section $\langle \sigma v \rangle$ versus the dark matter mass are shown in figure 15(b) and 15(d) together with the CTA sensitivity. For both BP1 and BP2, the predicted indirect detection cross-section from the GM-S model is larger than the expected reach from CTA in most of the mass range. The only region where the predicted cross-section is below the reach for CTA corresponds to $M_S < 227\,(200)$ GeV for BP1 (BP2). In this region, the pair production of new scalars is not kinematically accessible at low velocities and the predicted $\langle \sigma v \rangle$ which involves only the SM final states drop significantly at $M_S \sim 227\,(200)$ GeV as can be seen in figure 15(b) 15(c) for BP1 (BP2). Note that the subsequent dips in the indirect detection cross-section occur around $M_S \sim 250$ and 300 GeV where $H_3 H_3$ and $H_5 H_5$ modes open up for BP1.
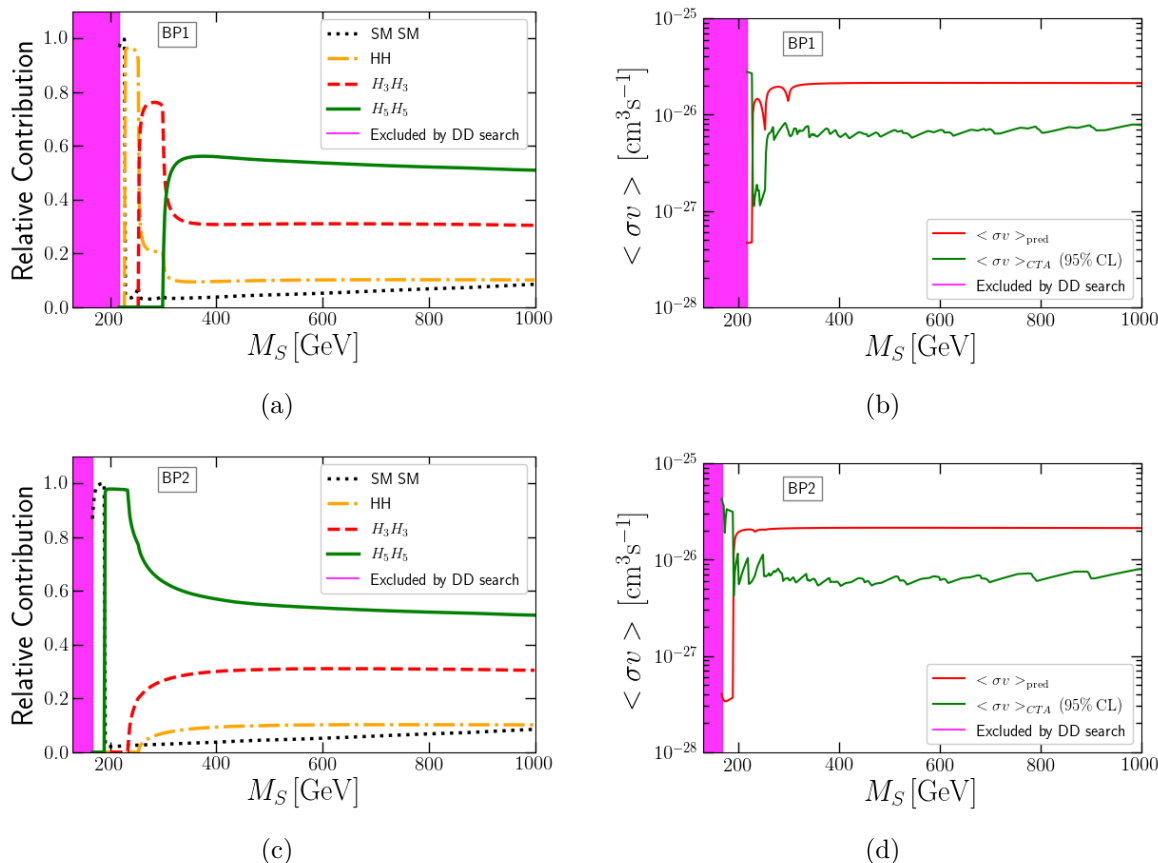
Figure 15. (a) Relative contribution of the DM pair annihilation and (b) CTA sensitivity for different DM masses for benchmark BP1; (c) Relative contribution of the DM pair annihilation and (d) CTA sensitivity for different DM masses for benchmark BP2. Note that all the points along the lines satisfy the observed DM relic density.

4.3 DM global scan

For all the points that satisfy the theoretical and experimental constraints discussed in previous sections which is about 1.4×10^3 allowed points, we have performed a global scan over the four parameters $\{\lambda_a, \lambda_b, \lambda_S, M_S\}$ relevant for DM production and detection, and computed the DM observables of the GM-S model. The total number of points sampled is about 3×10^5. We ensure that the points satisfy the theoretical constraints discussed in section 3.1. Moreover for these points $H \to SS$ is kinematically forbidden. Figure 16(a) shows the variation of the relic density versus $\frac{\lambda_b - \lambda_a}{\lambda_b}$ after imposing the direct detection constraint from LZ. The red points denote the points satisfying thermal relic within 2σ of the PLANCK measurement. As discussed above, as $\frac{\lambda_a}{\lambda_b}$ decreases, the relic density decreases leading to a large region of the parameter space being underabundant due to the proliferation of the relative contribution of the different BSM modes as shown in figure 16(b). In the following, we keep only points for which $\Omega_S h^2 > 0.001$ such that the singlet constitutes roughly, at least 1% of DM. As discussed above, see also figure 17, the DD constraint forces λ_a to be small and we find that in general $\lambda_a/\lambda_b < 1$. There are only a few points with $\lambda_a > \lambda_b$ which are associated with TeV scale DM where the DD constraint is weaker.
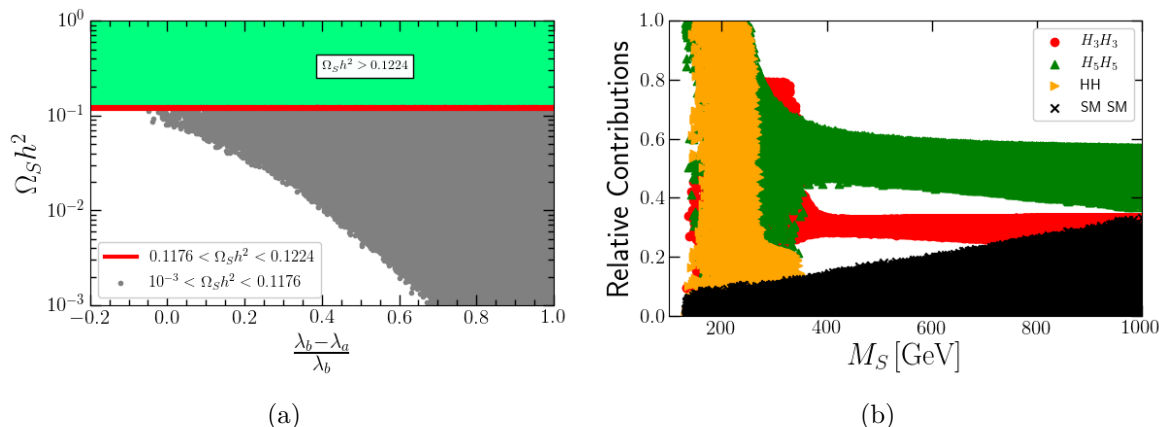
Figure 16. (a) Variation of DM relic abundance $\Omega_S h^2$ vs $\frac{\lambda_b - \lambda_a}{\lambda_b}$ after imposing the constraint from LZ, (b) relative contribution of different annihilation channels vs. M_S.

This implies that there is an important contribution from DM annihilation channels to BSM states over the entire allowed parameter space. Figure 16(b) shows that the relative contribution of DM annihilation to SM particles is always less than 30% for the entire DM mass range, and is less than 10% for $M_S < 200\,\mathrm{GeV}$ corresponding to the region where the DD constraint is strongest. It also shows that $H_5 H_5$ channels are the dominant BSM modes for $M_S > 370\,\mathrm{GeV}$ while any of the three modes HH, $H_3 H_3$ and $H_5 H_5$ can be dominant when $M_S < 340\,\mathrm{GeV}$.

In figure 17, we show the impact of the spin-independent direct detection cross-section on λ_a versus the DM mass M_S with $\zeta = \Omega_S h^2/0.12$ in the coloured palette. We can infer that values of $\lambda_a > 10^{-3}$ are excluded by LZ [56] for lower DM masses while the lower limit $\lambda_a > 5 \times 10^{-2}$ applies at $M_S = 1\,\mathrm{TeV}$. For lower values of λ_a, both DD and relic density constraints are satisfied. Moreover some of the lower values of λ_a remain well within the ambit of future direct detection experiments such as XENONnT and DARWIN while a fraction of the parameter space remains out of reach of future experiments. Note that as M_S approaches the TeV scale, we find a large number of points where the relic density is within the range measured by PLANCK ($\zeta \approx 1$). Since we work in the decoupling limit such that the BSM Higgs does not couple to SM fermions, λ_b remains unconstrained from direct detection searches.

Following the procedure described in the previous section, we also explored the sensitivity of indirect detection experiments. As expected, we found that the current Fermi-LAT data does not constrain the GM-S model since the typical annihilation cross-section ($\langle \sigma v \rangle \approx 3 \times 10^{-26}\mathrm{cm}^3/\mathrm{s}$) is much below the Fermi-LAT limit for DM masses above $100\,\mathrm{GeV}$. On the other hand, CTA will have the potential to probe a fraction of the parameter space of the GM-S model. Figure 18 shows the sensitivity of the DM pair annihilation cross-section at CTA versus the dark matter mass M_S. The predicted cross-section is scaled by the square of the DM fraction (ζ^2) and compared to the cross-section that can be reached by CTA including all DM annihilation channels into photons. The values of λ_b are shown in the color bar. The sensitivity ($\zeta^2 \langle \sigma v \rangle / \langle \sigma v \rangle_{\mathrm{CTA}}$) can exceed 1 for the whole range of DM masses. Many points are however beyond the reach of CTA, typically they correspond to underabundant DM ($\zeta \ll 1$)
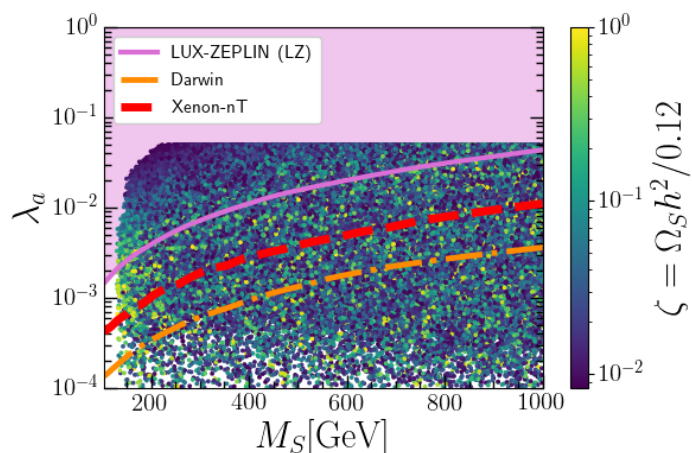
Figure 17. Impact of the constraint from DD searches from LZ (pink solid line) and projected reach of XENONnT [57] and DARWIN [58] shown by the red dashed and orange dash-dotted lines, respectively. The colour pallet corresponds to the ratio of predicted dark matter relic abundance and observed dark matter relic abundance.

found for the larger values of λ_b. In fact we found that in general, points where $\Omega_S h^2 \approx 0.12$ were well within reach of CTA. The only exception is found in the region $M_S \approx 200$ GeV when the DM mass is close to either M_H, M_{H_3} or M_{H_5} due to threshold effects. In these cases the annihilation channels into any pair of BSM scalars can contribute significantly to the relic density, but they have a negligible contribution at the lower velocities relevant for indirect detection. Therefore only SM final states are accessible and $\langle \sigma v \rangle$ for Indirect Detection (ID) is much suppressed. Note however that there is also a peak in the sensitivity around $M_S \sim 200$ GeV in figure 18(a), this corresponds to DM annihilating dominantly into HH as shown by the red points in figure 18(b). For higher values of the dark matter mass, the $H_3 H_3$ and $H_5 H_5$ channels open up and again there can be a significant increase in sensitivity although it never exceeds 4. We conclude that, while λ_b is unconstrained from direct detection data, future observations may constrain λ_b substantially.

5 Future prospects at colliders

In this section, we briefly discuss the discovery prospect of the BSM Higgs H_5^0 at the high-luminosity run of the LHC, focusing on the diphoton channel. As discussed in previous sections, current theoretical and experimental constraints restrict the mass of the new scalars in a relatively narrow range, namely 140 GeV $< M_{H_5} <$ 350 GeV, 150 GeV $< M_{H_3} <$ 270 GeV and 145 GeV $< M_H <$ 300 GeV. These are well within the range of the LHC, hence we investigate in this section the prospects of searches for these new scalars at the HL-LHC. In section 3, we have shown that current searches for $H^{\pm\pm} \to W^{\pm} W^{\pm}$ rule out the parameter space where this decay channel is dominant. Hence, for the doubly charged Higgs, one would need to investigate $H_5^{\pm\pm} \to H_3^{\pm} W^{\pm}$ and its cascade decays which lead to multi-leptons final states. However, the leptons being soft, this channel is challenging. A potentially more promising channel is the one with $H_i \to \gamma\gamma$ leading to a clean high p_T diphoton signature. Although both H_5^0 and H can decay into diphotons, as an example in this work we will consid er only $H_5^0 \to \gamma\gamma$.
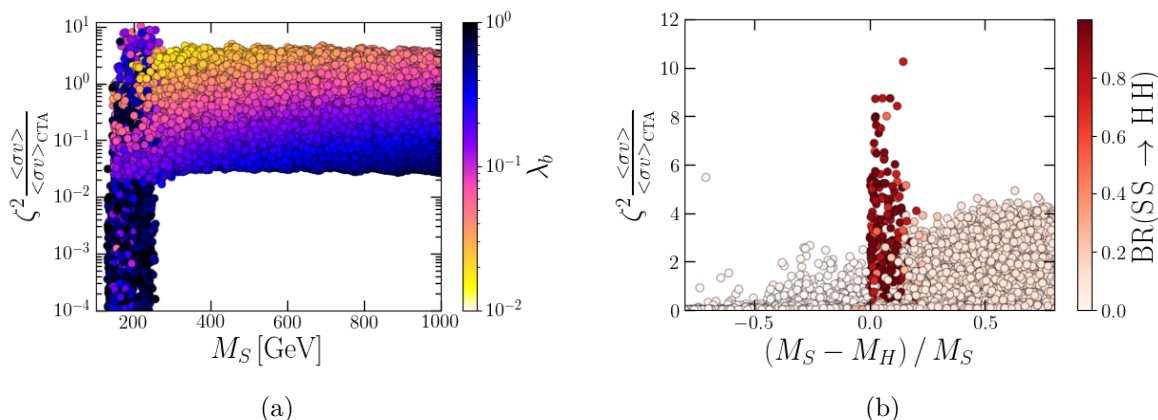
Figure 18. Ratio of the rescaled predicted cross-section to the 95% reach of CTA as a function of (a) M_S with λ_b in the color palette and (b) $(M_S - M_H)/M_S$ with the fraction of DM pair annihilation into HH in the color palette.
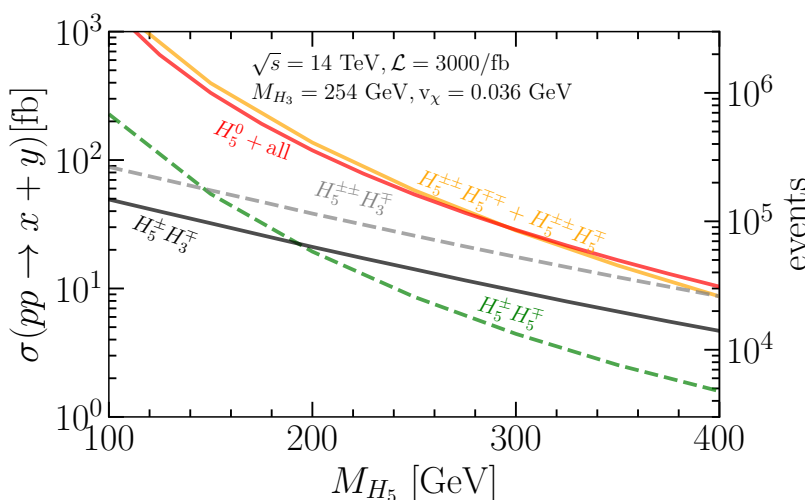

Figure 19. Production cross section (pair and associated) of BSM Higgs states as a function of M_{H_5} for $M_{H_3} = 254$ GeV and $v_\chi = 0.036$ GeV. Here, $pp \to H_5^0 + all$, represents $pp \to H_5^0 + \{V, H_5^\pm, H_3^\pm, H_3^0, H_5^0\}$. The right y-axis represents the number of events obtained for an integrated luminosity $\mathcal{L} = 3000$/fb.

Before proceeding further with a complete analysis of the diphoton projection for HL-LHC, we show in figure 19 the production cross sections (and the number of events along the right y-axis) as a function of M_{H_5} for a number of processes involving at least one member of the fiveplet. Here we fix $M_{H_3} = 254$ GeV and $v_\chi = 0.036$ GeV corresponding to one of the benchmarks (BP1) considered in section 4 to study DM production and detection. Note that all the processes shown are driven by DY so independent of v_χ). The number of events correspond to an integrated luminosity $\mathcal{L} = 3000$ fb^{-1} for HL-LHC. In the following, we analyse the diphoton signal from the process $pp \to H_5^0 + all$, which includes production of H_5^0 in association with $V, H_5^\pm, H_3^\pm, H_3^0, H_5^0$, with the dominant contribution coming from $pp \to H_5^0 H_5^\pm$.

We consider the two benchmark points defined in table 5. These are chosen among the allowed points in figure 9, for BP1 M_{H_5} is near the maximum value allowed while for

	M_{H_5} [GeV]	M_{H_3} [GeV]	v_χ [GeV]	M [GeV]	BR($H_5^0 \to \gamma\gamma$)	$\Gamma(H_5^0)$ [GeV]
BP1	300	254	0.036	335	0.59	45.7
BP2	190	234	0.05	210	0.70	3.8

Table 5. Benchmark points along with respective branching ratio of the decay channel $H_5^0 \to \gamma\gamma$ and total decay width of H_5^0.
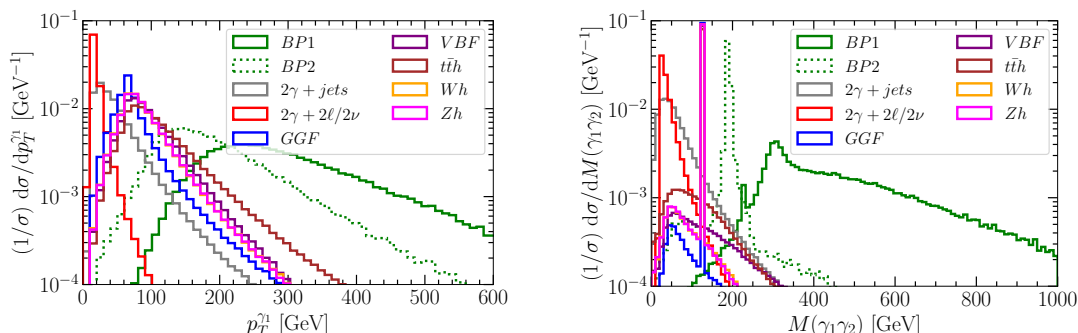
Figure 20. Distribution of transverse momentum $p_T^{\gamma_1}$ of the leading photon and invariant mass of the leading and sub-leading photon $M(\gamma_1\gamma_2)$ for signal and background.

σ^s (pb)		σ^b (pb)						
BP1	BP2	GGF	VBF	Zh	Wh	$t\bar{t}h$	$\gamma\gamma + 2\ell(2\nu)$	$\gamma\gamma + jets$
0.0167	0.0976	49.6	4.26	0.9	1.5	0.6	156.8	128.34

Table 6. Signal and background cross sections before applying selection cuts.

BP2 features a much lighter fiveplet. Both points have a rather large branching ratio into two photons, Br($H_5^0 \to \gamma\gamma$) > 50%. Moreover, both points are consistent with the dark matter constraints discussed in section 4.

The production process of H_5^0 at the HL-LHC is dominated by $pp \to H_5^0 H_5^\pm$. The cross-section followed by $H_5^0 \to \gamma\gamma$, is $\sigma = 0.0167$ pb and 0.0976 pb for BP1 and BP2, respectively. For the signal, we consider the two-photon final state arising from the decay of H_5^0. For BP1 we also consider cascade decays of $H_5^\pm$ state that give rise to multi-photon final states, namely

$$\text{BP1} : pp \to H_5^0 + H_5^\pm \to 2\gamma + W^\pm H_3^0 (Z H_3^\pm) \to 2\gamma + W^\pm + ZH \to 3(4)\gamma + X \quad (5.1)$$
$$\text{BP2} : pp \to H_5^0 + H_5^\pm \to 2\gamma + ZW \to 2\gamma + X$$

In the above decay chain for BP1, the branching ratios for $H_5^\pm \to W^\pm H_3^0$ and $H_3^0 \to ZH$ are nearly 100%, moreover the branching ratios for $H \to \gamma\gamma$ and $H \to \gamma Z$ reach together almost 100%. For BP2, the primary decay mode of $H_5^\pm$ is ZW with 100% branching ratio.

In the following, we implement a strong invariant mass cut around M_{H_5} to select only those events originating from H_5^0. Hence, an accurate reconstruction of the diphoton invariant mass can enhance the signal sensitivity. The photons are hard which facilitates event selection via a diphoton trigger [45].

We simulate signal and background events with MadGraph5amc@NLOv3.5.1 [65]. The dominant background for diphoton is $pp \to \gamma\gamma$. As our signal contains soft leptons and jets

in association with two or more photons, we consider other background processes such as $pp \to \gamma\gamma + 2l/2\nu/jets$ as well as SM Higgs production channels via gluon-fusion (GGF), vector boson fusion (VBF) and $Wh, Zh, t\bar{t}h$, and its decay to diphoton final state. Note that the background $pp \to \gamma\gamma + 2\ell(2\nu)$ does not involve the contribution from $pp \to Zh \to 2\ell + 2\gamma$, the latter is therefore generated separately. In table 6, we present the partonic cross-section for the signal $pp \to H_5^0 + all$, followed by H_5^0 decay to diphoton and for the SM background processes. The process $\gamma\gamma + 2l(2\nu)$ includes $pp \to \gamma\gamma$, $pp \to \gamma\gamma + 2\ell$ and $pp \to \gamma\gamma + 2\nu$, while $\gamma\gamma + jets$ includes $pp \to \gamma\gamma + 1jet$ and $pp \to \gamma\gamma + 2jets$. At the parton level we impose the following cuts, $p_T^{\gamma,\ell} \geq 10\,\mathrm{GeV}$, $p_T^{j} \geq 20\,\mathrm{GeV}$, $|\eta^{\gamma,\ell}| \leq 2.5, |\eta^{j}| \leq 5$. Note that, for signal, the cross-section presented in table 6 includes $H_5^0 \to \gamma\gamma$ branching ratio, while for backgrounds involving SM Higgs boson, we only show the production cross-section for $gg \to h, pp \to Zh, Wh$ and $t\bar{t}h$. The background cross sections involving the SM Higgs state are taken from [66] and have been multiplied with $\mathrm{Br}(h \to \gamma\gamma) = 0.25\%$.

The parton level events are passed to PYTHIA8.306 [67] to simulate parton shower and hadronization. In figure 20, we present the distributions of transverse momentum $p_T^{\gamma_1}$ for the leading photon and of the invariant mass of the leading and sub-leading photon $M(\gamma_1\gamma_2)$. As can be seen, the majority of the signal events populate the region $p_T^{\gamma_1} > 100$ GeV whereas, the SM backgrounds peak in the region $p_T^{\gamma_1} < 100$ GeV. Thus, we expect p_T cuts on the leading and sub-leading photon to reduce the background as discussed below. The $M(\gamma_1\gamma_2)$ distribution in figure 20 shows that the signal peaks at $M(\gamma_1\gamma_2) \sim M_{H_5}$. Therefore, a mass window around M_{H_5} is required to select the signal events. Note that for BP1, where H can arise from the cascade decay of $H_5^{\pm}$, there is a small peak around M_H which is due to $H \to 2\gamma$, as can be seen from the solid green line in the right panel of figure 20. After analysing the kinematics of the signal and background we consider the following sets of cuts to evaluate the signal sensitivity.

- $c_1 :$ $N^{\gamma} \geq 2$

- $c_2 :$ $c_1 + \{p_T^{\gamma_{1,2}} \geq 80, 30 \text{ GeV}, |\eta^{\gamma_{1,2}}| < 2.37 \}$

- $c_3 :$ c_2+isolation[5] for $\gamma_{1,2}$

- $c_4 :$ $c_3 + \{$ Reject event with $1.37 < |\eta^{\gamma_{1,2}}| < 1.52 \}$

- $c_5 :$ $c_4 + |M(\gamma_1\gamma_2) - M_{H_5}| = \pm 20\,\mathrm{GeV}$

We present a detailed cut-flow table for the two benchmark points and the SM backgrounds in table 7. As can be seen from this table, the signal cross-section is strongly suppressed for BP1, the global cut-efficiency is 11%, while for BP2 the global cut-efficiency is much better, 56%. The reason is that the $M(\gamma_1\gamma_2)$ distribution features a much narrower peak for BP2 than for BP1, see figure 20, right panel. We find that after cuts $\sigma^s = 1.8 \times 10^{-3}(0.054)$ pb for BP1 (BP2). After implementing the selection cuts, the largest background comes from $2\gamma + 2\ell/2\nu$ followed by $\gamma\gamma + jets$. We calculate the signal significance as $\mathcal{S} = N^s/\sqrt{N^s + N^b + (N^b\delta b)^2}$, where N^s (N^b) is the signal (background) events with $\mathcal{L} = 3000/\mathrm{fb}$ and δb is the background

---

[5]For isolation, we demand that the scalar sum of p_T of all the stable particles (except neutrinos) found within a $\Delta R = 0.4$ cone around the photon direction is required to be less than 0.05 $p_T + 6\,\mathrm{GeV}$.

	ϵ for signal		ϵ for backgrounds					
	BP1	BP2	GGF	VBF	Zh	Wh	$t\bar{t}h$	$2\gamma + 2\ell/2\nu \ (+jets)$
c_1	0.99	0.99	1.0	1.0	1.0	1.0	1.0	1.0 (0.99)
c_2	0.93	0.72	0.18	0.36	0.29	0.29	0.49	0.07 (6.10^{-3})
c_3	0.69	0.62	0.17	0.33	0.26	0.25	0.30	0.05 (6.10^{-3})
c_4	0.69	0.61	0.17	0.32	0.25	0.25	0.29	0.05 (6.10^{-3})
c_5	0.11	-	$1.1.10^{-5}$	10^{-4}	$6.5.10^{-5}$	$8.8.10^{-5}$	10^{-4}	0.002 (10^{-4})
c_5	-	0.56	$2.3.10^{-5}$	$3.0.10^{-4}$	$2.0.10^{-4}$	$3.0.10^{-4}$	$3.4.10^{-4}$	$7.8.10^{-3}$ ($1.5.10^{-3}$)
Events with $\mathcal{L} = 3000/\text{fb}$, $\mathcal{S} = N^s/\sqrt{N^s + N^b + (N^b\delta b)^2}$								
BP1				BP2				
$N^s = 5711$, $N^b = 1032684$, $\mathcal{S} = 0.55$				$N^s = 164434$, $N^b = 3758548$, $\mathcal{S} = 4.36$				

Table 7. Cut efficiency ϵ for signal and background.

uncertainty considered to be 1%. As shown in table 7, $\mathcal{S} = 0.55$ and $\mathcal{S} = 4.3$ can be obtained for BP1 and BP2, respectively.

We, therefore, conclude that the heavier H_5^0 could not be probed at the HL-LHC via the two-photon channel while scenarios with lighter H_5^0 such as in BP2 offer better prospects. Note that optimized cuts and advanced signal identification techniques should improve the significance determined here.

6 Summary and conclusion

In this work, we studied the collider and dark matter phenomenology of the GM-S model, a singlet extension of the Georgi-Machacek model, in its decoupling limit. In this limit, the common vev of the $Y = 0$ and $Y = 2$ triplets, v_χ, is very small. Based upon the transformation properties under the custodial symmetry, the physical scalars can be categorized into a fiveplet ($H_5^{\pm\pm}$, $H_5^\pm$ and H_5^0), a triplet ($H_3^\pm$ and H_3^0) and two CP-even singlets (H, h). In the decoupling limit, the mixing between h and H is identically zero as imposed by perturbative unitarity of the quartic couplings. We performed a comprehensive study by taking into account theoretical constraints (arising from, e.g., perturbative unitarity), measurement of oblique parameters, direct experimental searches/measurements at the LHC, such as, Higgs-to-diphoton rate measurements at the LHC, searches for a doubly charged Higgs and for heavy resonances decaying into diphotons at the 13 TeV LHC. We find that:

- Perturbative unitarity imposes an upper bound on the masses of the triplet and fiveplet, $M_{H_3} < 280$ GeV, and $M_{H_5} < 435$ GeV while oblique parameters measurements forbid a large mass splitting between these two states.

- The charged scalars can give a significant contribution to the diphoton decay width of neutral scalars. Agreement with LHC measurements of the $h \to \gamma\gamma$ rate imposes that $M_{H_5} - M \lesssim 30$ GeV, while requiring that the total widths of the BSM scalars satisfy $\Gamma(H_i)/M_i < 0.5$ leads to $v_\chi > 4.8 \times 10^{-3}$ GeV.

- In the allowed scenarios, the same-sign di-boson ATLAS search for doubly charged Higgs constrains the region where $M_{H_5} \sim 200 - 300$ GeV and $M_{H_3} \sim M_{H_5}$.

- The ATLAS search for heavy spin-0 resonances decaying into diphoton final states from Run 2 rules out $M_{H_3}\,(M_{H_5}) < 150\,(140)\,\mathrm{GeV}$. Moreover, it imposes a lower bound on v_χ of $v_\chi \geq 0.05\,\mathrm{GeV}$.

For the scan points that satisfy these theoretical and collider constraints, we performed an additional scan on the dark matter parameters, imposing constraints from the observed DM relic density as well as direct and indirect DM detection experiments. Our major findings are:

- The quartic coupling λ_a is severely constrained from the direct detection limit by LUX-ZEPLIN [56]. As a consequence, the dominant contribution to the DM relic density comes from the annihilation channels $SS \to HH, H_5H_5, H_3H_3$, which depend on λ_b.

- The presence of new scalars that can be produced in DM pair annihilation, $SS \to H_5H_5, HH, H_3H_3$, improve the DM indirect detection prospects as the direct decay $H_5^0, H \to \gamma\gamma$ can induce a harder photon spectra as compared to SM final state. This significantly improves the prospect for CTA to probe the model.

Last but not the least, we chose two benchmark points corresponding to $M_{H_5} = 190$ and $300\,\mathrm{GeV}$ and large $\mathrm{BR}(H_5^0 \to \gamma\gamma)$ and explored the detection prospects at the High-Luminosity run of the LHC. For the lighter point, $M_{H_5} = 190\,\mathrm{GeV}$, we found a significance of $> 4\sigma$ in final states with at least two photons.

In conclusion, the GM-S model in the decoupling limit offers a rich phenomenology that may be probed in near future direct and indirect detection experiments as well as at the high-luminosity run of the LHC. Note finally, that we only considered DM masses $\geq 100\,\mathrm{GeV}$, for which the observed SM-like Higgs boson cannot decay invisibly. The possibility of invisible Higgs decays in the GM-S model is left for future work.

Acknowledgments

A Partial decay widths of BSM scalars

In the following we present the general formulae for the partial decay widths of scalar H_I [15, 36].

$$\Gamma(H_I \to l_i^\pm l_j^\pm) = \frac{M_{H_I}}{8\pi} \left\{ \left[1 - (x_i + x_j)^2\right] |g^S|^2 + \left[1 - (x_i - x_j)^2\right] |g^P|^2 \right\} \lambda^{1/2}(x_i^2, x_j^2)$$

$$\Gamma(H_I \to V_1 V_2) = \mathcal{S} \frac{|g_{H_I V_1 V_2}|^2 M_{H_I}^3}{64\pi M_{V_1}^2 M_{V_2}^2} \left[1 - 2k_1 - 2k_2 + 10k_1 k_2 + k_1^2 + k_2^2\right] \lambda^{1/2}(k_1, k_2)$$

$$\Gamma(H_I \to V H_2) = \frac{|g_{V H_I H_2}|^2 M_V^2}{16\pi M_{H_I}} \lambda \left(\frac{M_{H_I}^2}{M_V^2}, \frac{M_{H_2}^2}{M_V^2}\right) \lambda^{1/2} \left(\frac{M_V^2}{M_{H_I}^2}, \frac{M_{H_2}^2}{M_{H_I}^2}\right)$$

$$\Gamma(H_I \to H_2 H_3) = \mathcal{S} \frac{|g_{H_I H_2 H_3}|^2}{16\pi M_{H_I}} \lambda^{1/2}(X_2, X_3) \tag{A.1}$$

In the above equations, $V = W^\pm, Z$ and H_I corresponds to BSM scalars. The couplings are $g^S = g^P = Y_{ij}^\nu$ while the kinematic quantities are given by $x_i = m_{l_i}/M_{H_I}$, $\lambda(x, y) = (1 - x - y)^2 - 4xy$, $k_i = M_{V_i}^2/M_{H_I}^2$, $X_i = M_{\Phi_i}^2/M_{H_I}^2$. $\mathcal{S}$ is a symmetry factor which takes values $\mathcal{S} = 1$ $(1/2)$ if final state particles are distinct (identical). Partial decay widths for off-shell decays are as follows

$$\Gamma(H_I \to VV^*) = \mathcal{S}\delta_V \frac{3|g_{H_I VV}|^2 M_{H_I}}{64\pi^3 v^2} \left[\frac{1 - 8k + 20k^2}{(4k-1)^{1/2}} \arccos \frac{3k-1}{2k^{3/2}} - \frac{1-k}{6k}(2 - 13k + 47k^2) \right.$$

$$\left. - \frac{1}{2}(1 - 6k + 4k^2)\log(k) \right],$$

$$\Gamma(H_I \to V^* H_2) = \delta_V \frac{3|g_{V H_I H_2}|^2 M_V^2 M_{H_I}}{16\pi^3 v^2} G_{H_2 V}, \tag{A.2}$$

where the factor δ_V and G_{ij} are given by,

$$\delta_W = 3/2,$$

$$\delta_Z = 3 \left(\frac{7}{12} - \frac{10}{9} \sin^2 \theta_W + \frac{40}{27} \sin^4 \theta_W\right),$$

$$G_{ij} = \frac{1}{4} \left\{ 2(-1 + k_j - k_i)\sqrt{\lambda_{ij}} \left[\frac{\pi}{2} + \arctan\left(\frac{k_j(1 - k_j + k_i) - \lambda_{ij}}{(1 - k_i)\sqrt{\lambda_{ij}}}\right)\right] \right.$$

$$\left. + (\lambda_{ij} - 2k_i)\log k_i + \frac{1}{3}(1 - k_i)\left[5(1 + k_i) - 4k_j + \frac{2\lambda_{ij}}{k_j}\right] \right\}. \tag{A.3}$$

In the above equation, $k_i = M_i^2/M_{H_I}^2$, and $\lambda_{ij} = -1 + 2k_i + 2k_j - (k_i - k_j)^2$. The vertex factor involved in the above decay width formula in the limit $s_\alpha = 0$ are given by

$$g_{HW^+W^-} = c_W^2 g_{HZZ} = \frac{4e^2 v_\chi}{\sqrt{3}s_W^2},$$

$$g_{H_5^0 W^+ W^-} = \sqrt{\frac{2}{3}} \frac{e^2}{s_W^2} v_\chi, \quad g_{H_5^0 ZZ} = -\sqrt{\frac{8}{3}} \frac{e^2}{s_W^2 c_W^2} v_\chi,$$

$$g_{H_5^+ W^- Z} = -\frac{\sqrt{2}e^2 v_\chi}{c_W s_W^2}, \quad g_{H_5^{++} W^- W^-} = \frac{2e^2 v_\chi}{s_W^2}. \tag{A.4}$$

$$g_{W^+hH_3^-} = -\sqrt{2}\frac{e}{s_W}\left(c_\alpha\frac{v_\chi}{v}\right), \quad g_{W^+HH_3^-} = -\sqrt{\frac{2}{3}}\frac{e}{s_W}\left(-c_\alpha\frac{v_\phi}{v}\right),$$

$$g_{W^+H_3^0H_5^-} = \frac{i}{2}\frac{e}{s_W}\frac{v_\phi}{v}, \quad g_{W^+H_3^+H_5^{--}} = \frac{1}{\sqrt{2}}\frac{e}{s_W}\frac{v_\phi}{v},$$

$$g_{ZhH_3^0} = -i\sqrt{2}\frac{e}{s_Wc_W}\left(\frac{v_\chi}{v}c_\alpha\right), \quad g_{ZHH_3^0} = i\sqrt{\frac{2}{3}}\frac{e}{s_Wc_W}\left(c_\alpha\frac{v_\phi}{v}\right),$$

$$g_{ZH_3^0H_5^0} = i\sqrt{\frac{1}{3}}\frac{e}{s_Wc_W}\frac{v_\phi}{v}, \quad g_{ZH_3^+H_5^-} = -\frac{e}{2s_Wc_W}\frac{v_\phi}{v},$$

$$g_{W^+H_3^-H_5^0} = -\frac{1}{2\sqrt{3}}\frac{e}{s_W}\frac{v_\phi}{v}. \tag{A.5}$$

$$g_{H_3^0H_3^0H_5^0} = -\frac{2\sqrt{2}}{\sqrt{3}v^2}\left(-8\lambda_5 v_\chi^3 + 4M_1 v_\chi^2 + (-4\lambda_5 + 2\lambda_3)v_\phi^2 v_\chi + 3M_2 v_\phi^2\right),$$

$$g_{H_3^+H_3^-H_5^0} = \frac{\sqrt{2}}{\sqrt{3}v^2}\left(-8\lambda_5 v_\chi^3 + 4M_1 v_\chi^2 + (-4\lambda_5 + 2\lambda_3)v_\phi^2 v_\chi + 3M_2 v_\phi^2\right),$$

$$g_{H_3^0H_3^+H_5^-} = -i\frac{\sqrt{2}}{v^2}\left(-8\lambda_5 v_\chi^3 + 4M_1 v_\chi^2 + (-4\lambda_5 + 2\lambda_3)v_\phi^2 v_\chi + 3M_2 v_\phi^2\right),$$

$$g_{H_3^+H_3^+H_5^{--}} = -\frac{2}{v^2}\left(-8\lambda_5 v_\chi^3 + 4M_1 v_\chi^2 + (-4\lambda_5 + 2\lambda_3)v_\phi^2 v_\chi + 3M_2 v_\phi^2\right),$$

$$g_{HH_5^0H_5^0} = g_{HH_5^+H_5^-} = g_{HH_5^{++}H_5^{--}} = 8\sqrt{3}\left(\lambda_3 + \lambda_4\right)v_\chi + 2\sqrt{3}\,M_2,$$

$$g_{HH_3^0H_3^0} = g_{HH_3^+H_3^-} = \frac{8}{\sqrt{3}}\frac{v_\phi^2 v_\chi}{v^2}\left(\lambda_3 + 3\lambda_4\right) + \frac{4}{\sqrt{3}}\frac{v_\chi^2 M_1}{v^2}$$

$$+ \frac{16}{\sqrt{3}}\frac{v_\chi^3}{v^2}\left(6\lambda_2 + \lambda_5\right) - \frac{2\sqrt{3}\,M_2 v_\phi^2}{v^2} + \frac{8}{\sqrt{3}}\lambda_5\frac{v_\chi v_\phi^2}{v^2}. \tag{A.6}$$

References

[1] CMS collaboration, *Observation of a New Boson at a Mass of 125 GeV with the CMS Experiment at the LHC*, *Phys. Lett. B* **716** (2012) 30 [`arXiv:1207.7235`] [INSPIRE].

[2] ATLAS collaboration, *Observation of a new particle in the search for the Standard Model Higgs boson with the ATLAS detector at the LHC*, *Phys. Lett. B* **716** (2012) 1 [`arXiv:1207.7214`] [INSPIRE].

[3] H. Georgi and M. Machacek, *Doubly Charged Higgs Bosons*, *Nucl. Phys. B* **262** (1985) 463 [INSPIRE].

[4] J.F. Gunion, R. Vega and J. Wudka, *Naturalness problems for $\rho = 1$ and other large one loop effects for a standard model Higgs sector containing triplet fields*, *Phys. Rev. D* **43** (1991) 2322 [INSPIRE].

[5] M.S. Chanowitz and M. Golden, *Higgs Boson Triplets With $M_W = M_Z \cos\theta_\omega$*, *Phys. Lett. B* **165** (1985) 105 [INSPIRE].

[6] H.E. Haber and H.E. Logan, *Radiative corrections to the $Z b\bar{b}$ vertex and constraints on extended Higgs sectors*, *Phys. Rev. D* **62** (2000) 015011 [`hep-ph/9909335`] [INSPIRE].

[7] M. Aoki and S. Kanemura, *Unitarity bounds in the Higgs model including triplet fields with custodial symmetry*, *Phys. Rev. D* **77** (2008) 095009 [*Erratum ibid.* **89** (2014) 059902] [`arXiv:0712.4053`] [INSPIRE].

[8] H.E. Logan and M.-A. Roy, *Higgs couplings in a model with triplets*, *Phys. Rev. D* **82** (2010) 115011 [`arXiv:1008.4869`] [INSPIRE].

[9] S. Chang, C.A. Newby, N. Raj and C. Wanotayaroj, *Revisiting Theories with Enhanced Higgs Couplings to Weak Gauge Bosons*, *Phys. Rev. D* **86** (2012) 095015 [`arXiv:1207.0493`] [INSPIRE].

[10] C.-W. Chiang and K. Yagyu, *Testing the custodial symmetry in the Higgs sector of the Georgi-Machacek model*, *JHEP* **01** (2013) 026 [`arXiv:1211.2658`] [INSPIRE].

[11] S. Kanemura, M. Kikuchi and K. Yagyu, *Probing exotic Higgs sectors from the precise measurement of Higgs boson couplings*, *Phys. Rev. D* **88** (2013) 015020 [`arXiv:1301.7303`] [INSPIRE].

[12] C. Englert, E. Re and M. Spannowsky, *Triplet Higgs boson collider phenomenology after the LHC*, *Phys. Rev. D* **87** (2013) 095014 [`arXiv:1302.6505`] [INSPIRE].

[13] C.-W. Chiang, A.-L. Kuo and K. Yagyu, *Enhancements of weak gauge boson scattering processes at the CERN LHC*, *JHEP* **10** (2013) 072 [`arXiv:1307.7526`] [INSPIRE].

[14] A. Efrati and Y. Nir, *What if* $\lambda_{hhh} \neq 3m_h^2/v$, [`arXiv:1401.0935`] [INSPIRE].

[15] K. Hartling, K. Kumar and H.E. Logan, *The decoupling limit in the Georgi-Machacek model*, *Phys. Rev. D* **90** (2014) 015007 [`arXiv:1404.2640`] [INSPIRE].

[16] R. Campbell, S. Godfrey, H.E. Logan and A. Poulin, *Real singlet scalar dark matter extension of the Georgi-Machacek model*, *Phys. Rev. D* **95** (2017) 016005 [`arXiv:1610.08097`] [INSPIRE].

[17] C. Degrande, K. Hartling and H.E. Logan, *Scalar decays to* $\gamma\gamma$, $Z\gamma$, *and* $W\gamma$ *in the Georgi-Machacek model*, *Phys. Rev. D* **96** (2017) 075013 [*Erratum ibid.* **98** (2018) 019901] [`arXiv:1708.08753`] [INSPIRE].

[18] N. Ghosh, S. Ghosh and I. Saha, *Charged Higgs boson searches in the Georgi-Machacek model at the LHC*, *Phys. Rev. D* **101** (2020) 015029 [`arXiv:1908.00396`] [INSPIRE].

[19] A. Ismail, H.E. Logan and Y. Wu, *Updated constraints on the Georgi-Machacek model from LHC Run 2*, [`arXiv:2003.02272`] [INSPIRE].

[20] A. Ismail, B. Keeshan, H.E. Logan and Y. Wu, *Benchmark for LHC searches for low-mass custodial fiveplet scalars in the Georgi-Machacek model*, *Phys. Rev. D* **103** (2021) 095010 [`arXiv:2003.05536`] [INSPIRE].

[21] Z. Bairi and A. Ahriche, *More constraints on the Georgi-Machacek model*, *Phys. Rev. D* **108** (2023) 055028 [`arXiv:2207.00142`] [INSPIRE].

[22] T.-K. Chen, C.-W. Chiang, C.-T. Huang and B.-Q. Lu, *Updated constraints on the Georgi-Machacek model and its electroweak phase transition and associated gravitational waves*, *Phys. Rev. D* **106** (2022) 055019 [`arXiv:2205.02064`] [INSPIRE].

[23] C.-W. Chiang, G. Cottin and O. Eberhardt, *Global fits in the Georgi-Machacek model*, *Phys. Rev. D* **99** (2019) 015001 [`arXiv:1807.10660`] [INSPIRE].

[24] C.H. de Lima and H.E. Logan, *Unavoidable Higgs coupling deviations in the Z2-symmetric Georgi-Machacek model*, *Phys. Rev. D* **106** (2022) 115020 [`arXiv:2209.08393`] [INSPIRE].

[25] V. Silveira and A. Zee, *Scalar Phantoms*, *Phys. Lett. B* **161** (1985) 136 [INSPIRE].

[26] J. McDonald, *Gauge singlet scalars as cold dark matter*, *Phys. Rev. D* **50** (1994) 3637 [hep-ph/0702143] [ɪɴSPIRE].

[27] C.P. Burgess, M. Pospelov and T. ter Veldhuis, *The minimal model of nonbaryonic dark matter: A Singlet scalar*, *Nucl. Phys. B* **619** (2001) 709 [hep-ph/0011335] [ɪɴSPIRE].

[28] GAMBIT collaboration, *Status of the scalar singlet dark matter model*, *Eur. Phys. J. C* **77** (2017) 568 [arXiv:1705.07931] [ɪɴSPIRE].

[29] B. Li, Z.-L. Han and Y. Liao, *Higgs production at future e^+e^- colliders in the Georgi-Machacek model*, *JHEP* **02** (2018) 007 [arXiv:1710.00184] [ɪɴSPIRE].

[30] D. Das and I. Saha, *Cornering variants of the Georgi-Machacek model using Higgs precision data*, *Phys. Rev. D* **98** (2018) 095010 [arXiv:1811.00979] [ɪɴSPIRE].

[31] H. Song, X. Wan and J.-H. Yu, *Custodial symmetry violation in scalar extensions of the standard model*, *Chin. Phys. C* **47** (2023) 103103 [arXiv:2211.01543] [ɪɴSPIRE].

[32] M. Chakraborti et al., *New physics implications of vector boson fusion searches exemplified through the Georgi-Machacek model*, *Phys. Rev. D* **109** (2024) 015016 [arXiv:2308.02384] [ɪɴSPIRE].

[33] A. Ahriche, *Constraining the Georgi-Machacek model with a light Higgs boson*, *Phys. Rev. D* **107** (2023) 015006 [arXiv:2212.11579] [ɪɴSPIRE].

[34] J. Chang, C.-R. Chen and C.-W. Chiang, *Higgs boson pair productions in the Georgi-Machacek model at the LHC*, *JHEP* **03** (2017) 137 [arXiv:1701.06291] [ɪɴSPIRE].

[35] T.-K. Chen, C.-W. Chiang and K. Yagyu, *Explanation of the W mass shift at CDF II in the extended Georgi-Machacek model*, *Phys. Rev. D* **106** (2022) 055035 [arXiv:2204.12898] [ɪɴSPIRE].

[36] K. Hartling, K. Kumar and H.E. Logan, *Indirect constraints on the Georgi-Machacek model and implications for Higgs boson couplings*, *Phys. Rev. D* **91** (2015) 015013 [arXiv:1410.5538] [ɪɴSPIRE].

[37] J.E. Camargo-Molina, B. O'Leary, W. Porod and F. Staub, *Vevacious: A Tool For Finding The Global Minima Of One-Loop Effective Potentials With Many Scalars*, *Eur. Phys. J. C* **73** (2013) 2588 [arXiv:1307.1477] [ɪɴSPIRE].

[38] C.-T. Lu, L. Wu, Y. Wu and B. Zhu, *Electroweak precision fit and new physics in light of the W boson mass*, *Phys. Rev. D* **106** (2022) 035034 [arXiv:2204.03796] [ɪɴSPIRE].

[39] J.F. Gunion, H.E. Haber, G.L. Kane and S. Dawson, *The Higgs Hunter's Guide*, Avalon Publishing (2000) [ɪɴSPIRE].

[40] ATLAS collaboration, *Measurement of the properties of Higgs boson production at $\sqrt{s} = 13$ TeV in the $H \to \gamma\gamma$ channel using $139\,fb^{-1}$ of pp collision data with the ATLAS experiment*, *JHEP* **07** (2023) 088 [arXiv:2207.00348] [ɪɴSPIRE].

[41] CMS collaboration, *Measurements of Higgs boson production cross sections and couplings in the diphoton decay channel at $\sqrt{s} = 13$ TeV*, *JHEP* **07** (2021) 027 [arXiv:2103.06956] [ɪɴSPIRE].

[42] ATLAS collaboration, *Search for doubly and singly charged Higgs bosons decaying into vector bosons in multi-lepton final states with the ATLAS detector using proton-proton collisions at $\sqrt{s} = 13$ TeV*, *JHEP* **06** (2021) 146 [arXiv:2101.11961] [ɪɴSPIRE].

[43] CMS collaboration, *Observation of electroweak production of same-sign W boson pairs in the two jet and two same-sign lepton final state in proton-proton collisions at $\sqrt{s} = 13$ TeV*, *Phys. Rev. Lett.* **120** (2018) 081801 [arXiv:1709.05822] [ɪɴSPIRE].

[44] ATLAS collaboration, *Search for doubly charged scalar bosons decaying into same-sign W boson pairs with the ATLAS detector*, *Eur. Phys. J. C* **79** (2019) 58 [arXiv:1808.01899] [INSPIRE].

[45] ATLAS collaboration, *Search for resonances decaying into photon pairs in 139 fb^{-1} of pp collisions at $\sqrt{s} = 13$ TeV with the ATLAS detector*, *Phys. Lett. B* **822** (2021) 136651 [arXiv:2102.13405] [INSPIRE].

[46] G. Alguero et al., *micrOMEGAs 6.0: N-component dark matter*, *Comput. Phys. Commun.* **299** (2024) 109133 [arXiv:2312.14894] [INSPIRE].

[47] A. Alloul et al., *FeynRules 2.0 — A complete toolbox for tree-level phenomenology*, *Comput. Phys. Commun.* **185** (2014) 2250 [arXiv:1310.1921] [INSPIRE].

[48] P. Gondolo and G. Gelmini, *Cosmic abundances of stable particles: Improved analysis*, *Nucl. Phys. B* **360** (1991) 145 [INSPIRE].

[49] E.W. Kolb, *The Early Universe*, Taylor and Francis (2019) [DOI:10.1201/9780429492860] [INSPIRE].

[50] G. Alguero, G. Bélanger, S. Kraml and A. Pukhov, *Co-scattering in micrOMEGAs: A case study for the singlet-triplet dark matter model*, *SciPost Phys.* **13** (2022) 124 [arXiv:2207.10536] [INSPIRE].

[51] PLANCK collaboration, *Planck 2018 results. VI. Cosmological parameters*, *Astron. Astrophys.* **641** (2020) A6 [*Erratum ibid.* **652** (2021) C4] [arXiv:1807.06209] [INSPIRE].

[52] W.-L. Guo and Y.-L. Wu, *The real singlet scalar dark matter model*, *JHEP* **10** (2010) 083 [arXiv:1006.2518] [INSPIRE].

[53] C. Armand and B. Herrmann, *Dark matter indirect detection limits from complete annihilation patterns*, *JCAP* **11** (2022) 055 [arXiv:2210.01220] [INSPIRE].

[54] A. Pukhov, *CalcHEP 2.3: MSSM, structure functions, event generation, batchs, and generation of matrix elements for other packages*, hep-ph/0412191 [INSPIRE].

[55] A. Belyaev, N.D. Christensen and A. Pukhov, *CalcHEP 3.4 for collider physics within and beyond the Standard Model*, *Comput. Phys. Commun.* **184** (2013) 1729 [arXiv:1207.6082] [INSPIRE].

[56] LZ collaboration, *First Dark Matter Search Results from the LUX-ZEPLIN (LZ) Experiment*, *Phys. Rev. Lett.* **131** (2023) 041002 [arXiv:2207.03764] [INSPIRE].

[57] XENON collaboration, *Physics reach of the XENON1T dark matter experiment*, *JCAP* **04** (2016) 027 [arXiv:1512.07501] [INSPIRE].

[58] DARWIN collaboration, *DARWIN: towards the ultimate dark matter detector*, *JCAP* **11** (2016) 017 [arXiv:1606.07001] [INSPIRE].

[59] P. Bhattacharjee, F. Calore, C. Eckner and P. Serpico, https://gitlab.in2p3.fr/christopher.eckner/mlfermilatdwarfs, (2023).

[60] MAGIC and FERMI-LAT collaborations, *Limits to Dark Matter Annihilation Cross-Section from a Combined Analysis of MAGIC and Fermi-LAT Observations of Dwarf Satellite Galaxies*, *JCAP* **02** (2016) 039 [arXiv:1601.06590] [INSPIRE].

[61] A. Reinert and M.W. Winkler, *A Precision Search for WIMPs with Charged Cosmic Rays*, *JCAP* **01** (2018) 055 [arXiv:1712.00002] [INSPIRE].

[62] CTA collaboration, *Sensitivity of the Cherenkov Telescope Array to a dark matter signal from the Galactic centre*, *JCAP* **01** (2021) 057 [arXiv:2007.16129] [INSPIRE].

[63] CTA CONSORTIUM and CTA OBSERVATORY collaborations, *The Cherenkov Telescope Array: layout, design and performance*, *PoS* **ICRC2021** (2021) 885 [arXiv:2108.04512] [INSPIRE].

[64] T. Miener et al., *Reconstruction of stereoscopic CTA events using deep learning with CTLearn*, *PoS* **ICRC2021** (2021) 730 [arXiv:2109.05809] [INSPIRE].

[65] J. Alwall et al., *The automated computation of tree-level and next-to-leading order differential cross sections, and their matching to parton shower simulations*, *JHEP* **07** (2014) 079 [arXiv:1405.0301] [INSPIRE].

[66] https://twiki.cern.ch/twiki/bin/view/LHCPhysics/CERNYellowReportPageAt14TeV.

[67] T. Sjostrand, S. Mrenna and P.Z. Skands, *A Brief Introduction to PYTHIA 8.1*, *Comput. Phys. Commun.* **178** (2008) 852 [arXiv:0710.3820] [INSPIRE].